SURFACE PLASMON POLARITON BANDWIDTH INCREASE USING CHIRPED-PITCH LINEAR DIFFRACTION GRATINGS FABRICATED ON AZOBENZENE THIN FILMS

AUGMENTATION DE LA BANDE DES POLARITONS DE PLASMON DE SURFACE AVEC DES RÉSEAUX LINÉAIRES À PAS VARIABLE INSCRITS DANS DES FILMS D'AZOBENZÈNE

A Thesis Submitted to the Division of Graduate Studies
of the Royal Military College of Canada
by

Erin K. Bailey

In Partial Fulfillment of the Requirements for the Degree of
Master of Science in Physics

October, 2017

Acknowledgements

I would like to thank my supervisor Dr. Ribal Georges Sabat, for his patience and guidance, as well as for teaching me inside and outside of the lab. I would also like to thank family and friends for their ongoing support.

Abstract

Surface plasmon polaritons that are excited by light incident on a diffraction grating are limited to discrete excitation wavelengths. Various applications could benefit from the simultaneous excitation of surface plasmons with a broad, bandwidth of wavelengths. To accomplish this, linear chirped-pitch surface relief grating were fabricated using a novel, single-step process whereby a chirped-pitch interference pattern was shone onto a photo-active azobenzene thin-film. To generate the chirped-pitch interference pattern, a modified Lloyd mirror set-up was used where a cylindrical lens was placed in front of the direct half of a 532 nm laser. Using this method, gratings with a chirping rate as high as (13.3 ± 0.8 nm/mm) were fabricated in 160 seconds. Then, by coating these gratings with a 60 nm layer of silver, surface plasmon polaritons were generated and measured by observing polarization dependent transmission peaks. When the full-width-half-max of these peaks was compared to that from constant-pitch gratings, an increase by a multiplicative factor ranging from 2.5 - 6 was observed, depending on the grating pitch.

Résumé

Les polaritons de plasmon de surface qui sont excités par la lumière incidente sur un réseau de diffraction sont limités à des longueurs d'onde discrètes. Diverses applications pourraient bénéficier de l'excitation simultanée des plasmons de surface avec une large bande de longueurs d'ondes. Pour ce faire, des réseaux de diffraction linéaires à pas variable ont été fabriqués à l'aide d'un nouveau procédé, ayant une seule étape de fabrication, à l'aide d'un patron d'interférence qui est incident sur un film d'azobenzène photo-actif. Pour générer le patron d'interférence à pas variable, une configuration modifiée du miroir de Lloyd a été utilisée avec une lentille cylindrique qui est placée devant la moitié directe du faisceau laser ayant une longueur d'onde de 532 nm. En utilisant cette méthode, des réseaux avec un taux de variation de pas aussi élevé que (13,3 +- 0,8 nm / mm) ont été fabriqués en 160 secondes. Ensuite, en recouvrant ces réseaux par une couche d'argent de 60 nm, des polaritons de plasmon de surface ont été générés et mesurés en observant les pics de transmission dépendants de la polarisation. Lorsque la largeur de bande de ces pics a été comparée à celle des réseaux à pas constant, une augmentation par un facteur multiplicatif allant de 2,5 à 6 fois a été observée, dépendant du pas du réseau.

Contents

List of Tables

List of Figures

List of Abbreviations

AFM	Atomic Force Microscope
CCD	Charge Coupled Device
DLIP	Direct Laser Interference Patterning
EM	Electromagnetic
FWHM	Full-width-half-max
rpm	revolutions per minute
SPP	Surface Plasmon Polariton
SPR	Surface Plasmon Resonance
TE	Transverse Electric (linearly polarized light)
TM	Transverse Magnetic (linearly polarized light)

List of Symbols

Greek Symbols

Symbol	Description	Definition
γ	Loss angle of a material.	$\arctan(\sigma/\epsilon\omega)$
δ	Phase difference between two light rays.	
ϵ	Dielectric permittivity of a material.	
ϵ_o	Dielectric permittivity of free space.	$\sim 8.854 \times 10^{-12}$ F·m^{-1}
ϵ_r	Relative dielectric permittivity of a material.	ϵ/ϵ_o
ε	Distance between the center of the direct half of the writing laser beam and the center of the cylindrical lens during grating fabrication.	
θ	Angle between writing laser beam and the surface of the mirror in the Lloyd mirror set-up.	
θ_i	Angle of incidence.	
θ_m	Angle of diffraction order.	
λ, λ_{light}	Wavelength of light.	
λ_{sp}	Surface plasmon wavelength.	
λ_{beam}	Wavelength of writing laser beam.	532 nm

Symbol	Description	Definition
μ	Magnetic permeability of a material.	
μ_o	Magnetic permeability of free space.	$\sim 1.257 \times 10^{-6}$ N$\cdot$/A^2
μ_r	Relative magnetic permeability of a material.	μ/μ_o
σ	Conductivity of a material.	
τ	Mean free path between electron collisions in a metal.	
ϕ	Phase shift between two light rays.	
ω	Angular frequency of light.	
ω_p	Plasmon frequency of a metal.	
ω_{sp}	Characteristic plasmon frequency	
Δ	Optical path difference between two light beams.	
Λ	Grating pitch.	

Roman Symbols

Symbol	Description	Definition
c	The speed of light in a vacuum.	$\sim 3.0 \times 10^8$m/s
D	Diameter of writing laser beam.	
$\vec{E}$	Electric field vector.	
$\vec{H}$	Magnetic field vector.	
I	Irradiance.	
j	Horizontal distance from the center of the cylindrical lens to a spot on a grating, in the grating fabrication set-up.	
k	wavenumber	$2\pi/\lambda$
K	Grating wavenumber	$2\pi/\Lambda$
L	Length of a grating.	$\mathrm{D}/2\cos\theta$
n	Refractive index of a material.	
$\hat{n}$	Unit vector normal to a surface.	
$\vec{r}$	position vector	
$\vec{s}$	Poynting vector (energy flux density).	

Additional Notation

Notation	Description
Q	Scalar
$\vec{Q}$	Vector
$\hat{Q}$	Unit vector
Q_x	x-component of the vector Q
Q_y	y-component of the vector Q
Q_z	z-component of the vector Q
$\tilde{Q}$	Complex number
Q'	Real part of $\tilde{Q}$
Q''	Imaginary part of $\tilde{Q}$
Q_d	Quantity in a dielectric
Q_m	Quantity in a metal
$< Q >$	Time-average of the varying value Q

1 Introduction

Surface plasmon resonance (SPR) waves are light induced, electron density fluctuations at the surface of a conductor [1, 2]. They are generated when the electromagnetic field (EM-field) from a light source causes the conduction electrons to collectively oscillate in resonance with the light's EM-field. These oscillating electrons in turn couple to the light, confining it to the surface.[3] Since both light and electronic charge are involved in a surface plasmon wave, the term surface plasmon polariton (SPP) was coined in 1972 by Stephan Cunningham et al.[4] to represent this dual nature. This term is still used today and is interchangeable with surface plasmon resonance (SPR) waves.

SPR waves occur at the boundary between two materials where the real part of the dielectric permittivity changes sign [1]. This condition is often met at the boundary between a metal and a dielectric, where the conduction electrons of the metal form the plasmonic wave. Depending on the materials involved and the wavelength of light, SPR waves can propagate on a smooth metallic surface for lengths on the order of micrometers [3] before dissipating as heat. In addition, the electric field perpendicular to the surface decays exponentially away from the surface, sometimes confining the SPP field to sub-wavelength scales. This high confinement leads to a large electric field amplitude along the surface [1].

1.1 History of Surface Plasmon Waves

SPR waves were first reported in 1902 by R.W. Wood [5] as unexplainable anomalies in the reflection spectra from a metallic diffraction grating. Narrow peaks and dips in an otherwise continuous spectrum were observed, but only when the electric field was polarized perpendicular to the grating grooves. These anomalies occurred at different wavelengths depending on the angle of incidence, as well as the dielectric material placed directly in front of the grating. Wood was not able to explain his observations using the diffraction theory of his time.

A few years later, in 1907, Lord Rayleigh [6] was able to connect Wood's anomalies to diffraction orders emerging at a grazing angle with respect to the grating. In doing so, he was able to predict the wavelengths for Wood's anoma-

lies (Rayleigh wavelengths) and explain the polarization dependence of the phenomenon. His theory however, was limited because it failed to produce the correct spectral shape for these anomalies [7].

It wasn't until 1941, that U. Fano [8] related Wood's anomalies to surface waves propagating along the interface between a metal and a dielectric. The mathematical framework for these surface waves had been laid out years earlier in 1899 and 1907 by Sommerfeld [9] and Zenneck[10], respectively. By 1965, Hessel and Oliner [7] had provided the accepted mathematical framework for the resonance phenomenon [11].

Additionally, in 1957, Ritchie [12] was able to excite self-sustained electron density fluctuations with fast electrons passing through thin metallic foils. In 1960, Powell and Swan [13] obtained electron energy loss spectra for thin aluminum and magnesium foils, and found that the energy of these losses shifted as the surface of the metal oxidized. Finally, by 1968, these electron loss spectra had been connected back to Woods anomalies by Ritchie et al. [14] and are described as a quantization of surface plasmon resonance. This connection completed the physical understanding of SPR waves.

1.2 Applications of Surface Plasmon Resonant Waves

Since their discovery, surface plasmon resonant waves have generated considerable attention across a wide variety of fields due to their ability to confine and guide light along the surface of a metal. This boom in research shows no sign of slowing down. The annual number of papers containing "Surface Plasmon" somewhere in their title or abstract has doubled every five years from 1990 to 2005 [2]. A large amount of this research is application-based, with the number of applications too large to be fully listed here.

Some applications make use of the sensitivity of the surface plasmon's dispersion relation to the surrounding dielectric material. If the refractive index of the dielectric changes in the vicinity of the metal surface, the excitation wavelength of the plasmon will change. This has allowed for the development of sensors capable of detecting a single layer of molecules chemically bound to a metallic surface [15].

Other applications include the enhancement of Raman scattering [16], fluorescent emission [17], and non-linear optical phenomenon like second harmonic generation [18]. The strength of these phenomena depends on the strength of the surrounding electric field. The highly localized, and therefore amplified electric field associated with surface plasmon resonance can amplify the signal from these processes.

Other applications fall into the realm of sub-wavelength optics, where the confinement of the electromagnetic field has the potential for optical imaging [19],

data storage [20] and optical lithography [21] below the diffraction limit imposed by conventional optical systems.

Finally, one of the most obvious applications for surface plasmon resonance is the guidance of light. The propagation direction of a SPR wave can be controlled via scattering along the surface of the metal [22]. In addition, the phase velocity of SPR waves can be locally modified by dielectric nano-structures at the metal-dielectric interface [1]. Optical elements analogous to lenses and prisms [23] can be made to focus or disperse these two-dimensional surface waves. This has potential use in planar photonic circuits.

Another place where the guiding of light energy can be taken advantage of is in thin film solar cells. If a SPR wave is excited along the interface of a metal electrode in a photo-active material, the light will spend a longer time in the photo-active material than if a SPR wave was not produced. This can increase the efficiency of a solar cell, without increasing the thickness of the photo-active layer [24].

1.3 Excitation Methods

Surface plasmon waves cannot be excited by simply shining light onto the surface of a metal [1–3]. The wave-vector of the surface plasmon, k_{sp}, is always larger than the wave-vector of incident light, k_{light}. In order to optically excite a surface plasmon, various methods can be used to match the wave-vector of incident light to that of the plasmon's along the direction of propagation.

One popular excitation method is through prism coupling, for which there exists two distinct excitation configurations. The Kretchmann method, shown in Fig.1.1-a was first used in 1968 by Kretchmann and Reather [25]. It involves coating a prism of some dielectric permittivity, ϵ_{prism}, with a thin metallic film. Light striking the prism-metal interface at an angle greater than the critical angle for total internal reflection, can tunnel through to the other side of the metal [1][26]. This tunnelling evanescent light can then excite surface plasmon waves on the other side of the metal, at the metal-dielectric interface, so long as the dielectric permittivity, ϵ_d, is smaller than the dielectric permittivity of the prism, $\epsilon_d < \epsilon_{prism}$ [26].

The Otto configuration, developed in 1968 by Andreas Otto [27], is shown in Fig.1.1-b. This method is very similar to the Kretchmann configuration. However, instead of coating the prism with a metal, the prism is placed close to a metal, with a thin dielectric material between the two. The evanescent wave generated by total internal reflection at the prism-dielectric interface can tunnel through the sandwiched dielectric to the metal, exciting a surface plasmon wave at the metal-dielectric interface [1].

Another common method for optical surface plasmon excitation is through scattering from defects along the surface of a metallic film [1][2]. Light striking a defect, as shown in Fig. 1.1-c, can be scattered in all directions and add an additional momentum component, Δk_x, to the incoming light, allowing for wave-vector matching. Already propagating SPR waves can also be de-excited by defects and re-emitted as light.

Finally, one of the earliest methods for exciting a SPR wave, already mentioned above in Section 1.1, is through the use of a metallic diffraction grating. Shown in Fig. 1.1-d below, if light is incident at an angle θ on a metallic diffraction grating with grating spacing Λ, and the light is polarized with a component of the electric field perpendicular to the grating's grooves, light that is diffracted along the grating's surface, will have an additional wave-vector component $K = \frac{2\pi}{\Lambda}$ [11]. This additional wave-vector can satisfy the wave-vector matching condition for certain wavelengths and angles of incidence, so that $k_{sp} = k \sin\theta + K$. Once coupled to the surface, SPR waves can also be re-emitted as light by this mechanism.

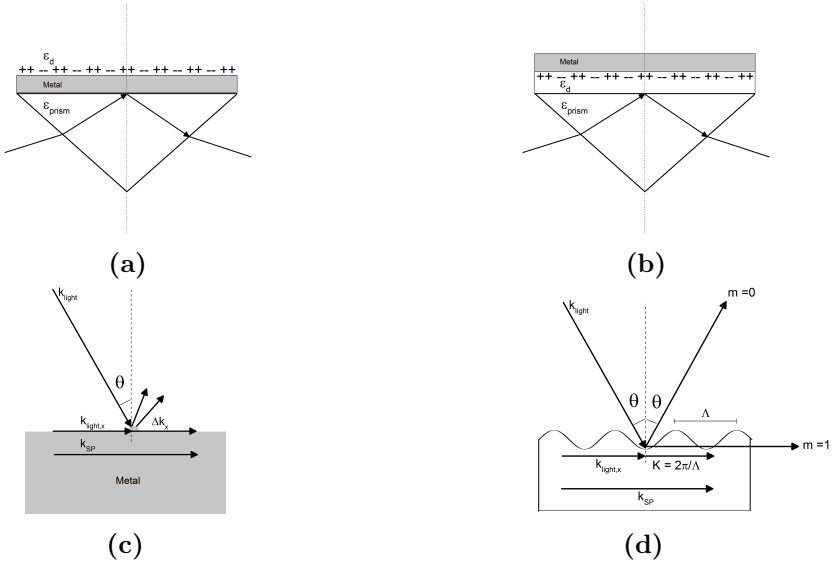

Figure 1.1: Four common methods of optically exciting surface plasmon resonant waves: (a)Kretchmann configuration, (b) Otto configuration,(c) scattering from a random defect, and (d) the grating method.

1.4 Non-linear Diffraction Gratings

Looking at the four methods for surface plasmon excitation discussed above, the grating method offers some obvious advantages over the other three methods. Compared to the two prism coupling methods, a two-dimensional, nano-structured

grating is much more compact. Also, with current lithography techniques, the depth and pitch of a grating can be precisely controlled, which in turn allows for excellent control over the surface plasmon propagation wavelength. However, one disadvantage is that only light polarized with the electric field perpendicular to the grating grooves will generate surface plasmon polaritons. Furthermore, only surface plasmons at a discrete wavelength, dependent on the angle of incidence, the grating spacing, and the refractive indices of the metal and dielectric, can be excited for each grating. This can be quite limiting for applications such as plasmonic enhanced absorption in thin film solar cells. Ideally, enhancement over all absorbing wavelengths of the photo-active material, and all polarization directions will allow for the greatest enhancement in solar cell efficiency. To overcome this, research has begun on non-conventional grating structures, such as compound, and non-periodic gratings that can couple multiple polarizations and surface plasmon wavelengths at the same time.

For example, to deal with the polarization limitation, curved [28] and circular grating structures [29–31] have been shown to couple multiple, if not all, polarization directions of incoming incident light when the light is of the correct wavelength for the grating spacing.

To couple multiple wavelengths into surface plasmons, "quasi-periodic" gratings that have long-range order but are not locally periodic have been constructed and tested by Dolev [32]. Specifically, these gratings were designed to have well defined peaks in their Fourier harmonic spectra. These Fourier harmonic gratings were found to efficiently couple multiple surface plasmon polaritons on the same grating structure.

In addition, compound gratings made of two parallel gratings, superimposed on top of each other, have been studied by Hillier [33], and here at RMCC by Jefferies and Sabat [34]. Broad-band photo-current enhancement in organic photovoltaic thin-films were observed with these gratings [34].

Both compound and Fourier harmonic gratings have been theoretically tested, using rigorous coupled wave-analysis, in silicon solar cells by Atalla [35, 36]. Here, it was found that a Fourier harmonic grating was more efficient in surface plasmon coupling than a compound grating.

Other groups have made perpendicular compound gratings, or crossed gratings [37, 38], where one grating is made by a laser interference lithography exposure, and another is made directly on top, by turning the sample 90° and performing another exposure. This method allows for two polarization directions to excite surface plasmons, and for multiple wavelength excitations if the two grating periods are different from each other. Furthermore, Dostalek et al. [38] was also able to superimpose three separate grating pitches (525 nm, 612 nm, and 690 nm), parallel to each other, then rotate the grating by 90° and superimpose the three grating pitches again, to make crossed multi-pitched gratings. This was found to

increase the absorption spectra of a photovoltaic material.

In current literature, chirped-pitch diffraction gratings, where the grating spacing gradually varies, have been constructed for other applications, such as optical trapping [39, 40], guided-mode resonance filters [41], resonance enhanced transmission [42], and optical beam focusing through a sub-wavelength slit [43]. Others have made chirped-pitch diffraction gratings to study the near-field behaviour of light incident on the gratings [44]. However, no one has looked for a potential band-width increase in the surface plasmon excitation wavelength.

1.5 Azobenzene Thin Films for Grating Construction

A useful tool for the fabrication of both conventional, single-pitched gratings, and some of the non-conventional gratings mentioned above in Section 1.4, are photo-active azobenzene containing polymers and glasses. The azobenzene molecule has two isomers with the chemical structure shown in Fig. 1.2 below. Depending on the functional groups attached to this azobenzene backbone, the molecule can undergo cis-trans isomerization upon absorption of a specific wavelength of light.

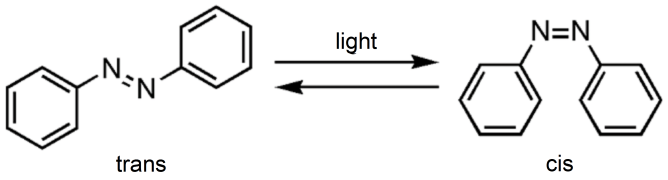

Figure 1.2: The different isomers of azobenzene.

When this photochemical reaction occurs in a thin-film of molecules, localized mass transport of the material can occur. This movement of molecules was found to be proportional to the second derivative of the absorbing light's intensity profile [45]. This means that if an interference pattern in shone on a photo-active azobenzene thin film, the interference pattern will be photo-mechanically imprinted onto the film.

This can be used to generate sinusoidal diffraction gratings in a single exposure in a matter of seconds, without any post-exposure processing [46]. Furthermore, gratings can be superimposed on top of each other by making sequential exposures [34]. Theoretically, any pattern of light that can be generated and shone onto a sample, can be photo-mechanically imprinted, making azobenzene materials highly versatile.

1.6 Thesis Statement

Surface plasmon polariton excitation across a broad bandwidth of wavelengths can be achieved using a chirped-pitch diffraction grating structure. These gratings can be fabricated using a novel method, direct laser interference patterning (DLIP) on azobenzene molecular glass thin films. This involves exposing an azobenzene film to an interference pattern with gradually varying spacings between the interference maxima, to create a chirped, sinusoidal grating. When these gratings are coated with silver, the silver conforms to the azobenzene grating [34], allowing for surface plasmon excitation at the silver-air interface. By comparing the full-width-half-max of transmission peaks from chirped-pitch gratings with that of constant-pitch gratings, a bandwidth increase will be demonstrated.

1.7 Structure of Thesis

This thesis will be divided into five main sections. Chapter 2 of the thesis covers relevant theory, starting with the electromagnetic wave description of light, as dictated by Maxwell's equations. An overview of irradiance, interference and the diffraction of light by diffraction gratings is then given. This is followed by a mathematical description of SPR waves and how they can be excited by light incident on a diffraction grating. Finally, a geometric description of the grating fabrication set-up is given for both constant-pitch gratings and chirped-pitch gratings.

Chapter 3 will discuss the grating fabrication process and testing procedures, as well as the different experimental set-ups used to generate the results of this thesis.

Chapter 4 is the results section of the thesis. It will start by going through optimization steps for both constant and chirped-pitch diffraction gratings before comparing the plasmonic response between the two types of gratings. In the process, results will be graphically represented and discussed at length.

Finally, Chapter 5 will be the conclusion. Here, results are summarized in relation to the goals of this thesis as well as work to be done in the future.

2 Theoretical Overview

This chapter will provide the reader with the necessary theory and mathematics to understand the work contained in this thesis. For completeness, theory will be presented from basic concepts and derived to their final form.

To begin, some fundamental properties of light and interference will be presented. Then the grating equation will be derived, so that it may be discussed in relation to the excitation of surface plasmons. Finally, the process of creating both regular and chirped gratings with a Lloyd mirror set-up will be geometrically analysed, so that the spacings of gratings can be predicted and compared to gratings fabricated in the lab.

2.1 Mathematical Representation of Light

2.1.1 Electromagnetic Waves in a Vacuum

Light can behave as both a wave and a particle, and depending on the application, one representation is often more useful than the other. In this thesis, light will be regarded exclusively as an electromagnetic wave described by Maxwell's equations. These are shown below for a wave in a vacuum (charge and current free), which is a good approximation for light travelling through air [47].

$$\nabla \cdot \vec{E} = 0 \tag{2.1.1a}$$

$$\nabla \times \vec{E} = -\mu_0 \frac{\partial \vec{H}}{\partial t} \tag{2.1.1b}$$

$$\nabla \cdot \vec{H} = 0 \tag{2.1.1c}$$

$$\nabla \times \vec{H} = \epsilon_0 \frac{\partial \vec{E}}{\partial t} \tag{2.1.1d}$$

Here, μ_0 is the magnetic permeability of free space, and ϵ_0 is the permittivity of free space. $\vec{E}$ is the electric field vector, and $\vec{H}$ is the magnetic field. As seen in Fig. 2.1 below, these fields are mutually perpendicular to each other and to the direction of travel, making them transverse waves. By convention, the electric

field, $\vec{E}$, dictates the polarization direction of the wave. In Fig. 2.1, the wave is linearly polarized, meaning the electric field vector does not change direction upon propagation. In this particular image, the wave is polarized in the $\hat{x}$ direction.

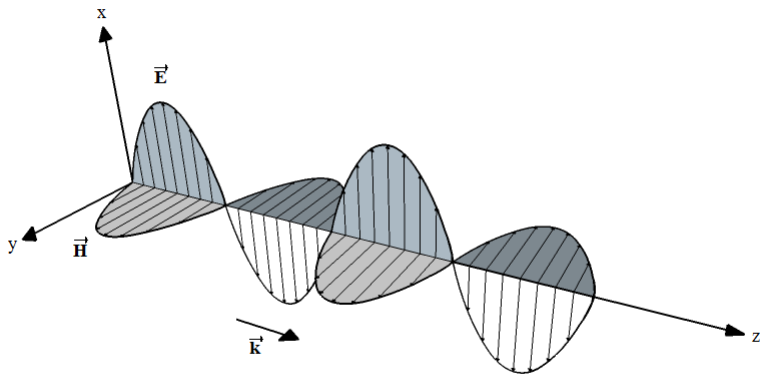

Figure 2.1: An electromagnetic wave polarized in the $\hat{x}$, propagating along the z-axis.

Taking the cross product of Eqs. 2.1.1-b and 2.1.1-d, and substituting in the other two equations 2.1.1-a and 2.1.1-c, one can arrive at the wave equations for both $\vec{E}$ and $\vec{H}$ [47].

$$\nabla^2 \vec{E} = \mu_0 \epsilon_0 \frac{\partial^2 \vec{E}}{\partial t^2} \tag{2.1.2}$$

$$\nabla^2 \vec{H} = \mu_0 \epsilon_0 \frac{\partial^2 \vec{H}}{\partial t^2} \tag{2.1.3}$$

From this, it can be seen that in a vacuum, light travels at the speed

$$c = \frac{1}{\sqrt{\mu_0 \epsilon_0}} = 3 \times 10^8 \text{ m/s} \tag{2.1.4}$$

The direction of propagation, $\vec{r}$, can be represented by the wave-vector, $\vec{k}$, where $|\vec{k}| = k = \frac{2\pi}{\lambda}$ is the wave-number [47]. If we assume harmonic, plane-wave solutions at position $\vec{r}$ and time t, we can write the electric and magnetic fields using complex notation. It is, however, understood that the physical fields, $\vec{E}$ and $\vec{H}$, are represented by the real parts of the complex fields, $\tilde{E}$ and $\tilde{H}$ [47]

$$\vec{E}(\vec{r},t) = Re\left\{\tilde{E}(\vec{r},t)\right\}\hat{n} \tag{2.1.5a}$$

$$\vec{H}(\vec{r},t) = Re\left\{\tilde{H}(\vec{r},t)\right\}(\hat{k}\times\hat{n}) \tag{2.1.5b}$$

Here, $\hat{n}$ is the unit vector in the direction of polarization, and $\hat{k}$ is the unit vector in the direction of travel. If the light waves have an angular frequency ω, given by the vacuum dispersion relation for light [47, 48],

$$\omega = ck, \tag{2.1.6}$$

then the complex wave functions are as shown below.

$$\tilde{E}(\vec{r},t) = \tilde{E}_0 e^{i(\vec{k}\cdot\vec{r}-\omega t)} \tag{2.1.7a}$$

$$\tilde{H}(\vec{r},t) = \tilde{H}_0 e^{i(\vec{k}\cdot\vec{r}-\omega t)} = \frac{\tilde{E}_0}{\mu_0 c} e^{i(\vec{k}\cdot\vec{r}-\omega t)} \tag{2.1.7b}$$

$\tilde{E}_0$ and $\tilde{H}_0$ are the complex amplitudes of the electric field and magnetic field, respectively.

2.1.2 Irradiance

When detecting an electromagnetic wave, the electric and magnetic fields are not measured directly. Instead, the irradiance, I, sometimes referred to as intensity of a beam, is measured. It is defined as the radiant flux density received by a surface in units of Watts/m^2. The irradiance of a light beam striking a surface at an angle α to the vector normal of the surface is [47–49],

$$I = \left\langle |\vec{S}| \right\rangle \cos\alpha, \tag{2.1.8}$$

where $\vec{S}$ is the energy flux density, also known as the Poynting vector. The Poynting vector can be described in terms of the cross product of the electric field and the magnetic field flux density [47–49].

$$\vec{S} = \vec{E} \times \vec{H} \tag{2.1.9}$$

The angular brackets, $\langle\ \rangle$, in Eq. 2.1.8 indicate that the time-average of the Poynting vector is being taken. This is because $\vec{E}$ and $\vec{H}$ vary rapidly compared to the time it takes for a typical detector to make a measurement [47, 48]. Substituting Eq. 2.1.9 into Eq. 2.1.8, and using Eq. 2.1.4 for the speed of light gives,

$$I = \epsilon_0 c \left\langle \vec{E}\cdot\vec{E} \right\rangle. \tag{2.1.10}$$

2.1.3 Interference of Beams

To see how the irradiance behaves when two or more beams of light interfere, it is helpful to look at Fig. 2.2 below.

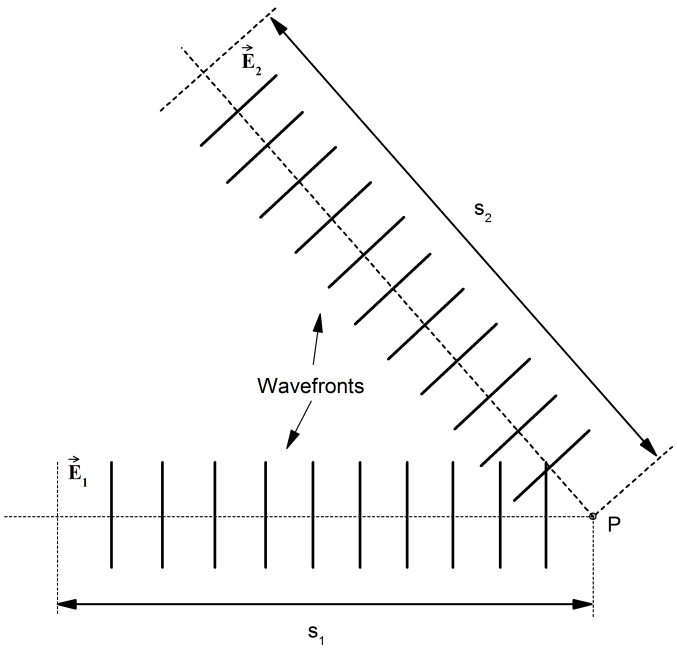

Figure 2.2: Two interfering plane waves.

Assuming $\vec{E}_1$ and $\vec{E}_2$ are two plane waves with the same frequency, the electric field at point P is given by the superposition principle [48] so that,

$$\vec{E}_P = \vec{E}_1 + \vec{E}_2 \tag{2.1.11}$$

where,

$$\vec{E}_1 = \vec{E}_{01}\cos\left(ks_1 - \omega t + \phi_1\right) \tag{2.1.12a}$$
$$\vec{E}_2 = \vec{E}_{02}\cos\left(ks_2 - \omega t + \phi_2\right) \tag{2.1.12b}$$

As shown in Fig. 2.2, s_1 and s_2 are the respective path lengths travelled by the two waves. At their source, when time $t = 0$, ϕ_1 and ϕ_2 are the respective phases of the two waves.

The irradiance at point P can be found by substituting Eq. 2.1.11 into Eq. 2.1.10, as shown below.

$$\begin{aligned} I_P &= \epsilon_0 c \left\langle \vec{E}_P \cdot \vec{E}_P \right\rangle \\ &= \epsilon_0 c \left\langle \left(\vec{E}_1 + \vec{E}_2\right) \cdot \left(\vec{E}_1 + \vec{E}_2\right) \right\rangle \\ &= \epsilon_0 c \left\langle \vec{E}_1 \cdot \vec{E}_1 + \vec{E}_2 \cdot \vec{E}_2 + 2\vec{E}_1 \cdot \vec{E}_2 \right\rangle \\ &= I_1 + I_2 + I_{12} \end{aligned} \tag{2.1.13}$$

Then, by substituting Eq. 2.1.12 into Eq. 2.1.13, we obtain for I_1,

$$\begin{aligned} I_1 &= \epsilon_0 c E_{01}^2 \left\langle \cos^2\left(ks_1 - \omega t + \phi_1\right)\right\rangle \\ &= \frac{1}{2}\epsilon_0 c E_{01}^2, \end{aligned} \tag{2.1.14}$$

where the time average of the square of any cosine function is 1/2.

Similarly,

$$I_2 = \frac{1}{2}\epsilon_0 c E_{02}^2 \tag{2.1.15}$$

For I_{12}, the trigonometric identity

$$2\cos(A)\cos(B) = \cos(A+B) + \cos(B-A) \tag{2.1.16}$$

is used to simplify the expression [48], giving

$$\begin{aligned} I_{12} &= 2\epsilon_0 c\vec{E}_{01}\cdot\vec{E}_{01}\left\langle \cos(ks_1 - \omega t + \phi_1)\cos(ks_2 - \omega t + \phi_2)\right\rangle \\ &= 2\epsilon_0 c\vec{E}_{01}\cdot\vec{E}_{01}\left\langle \cos(k(s_1+s_2) + \phi_1 + \phi_2 - 2\omega t) + \cos(k(s_2 - s_1) + \phi_2 - \phi_1)\right\rangle \\ &= 0 + \sqrt{I_1 I_2}\left\langle \cos(\delta)\right\rangle \end{aligned} \tag{2.1.17}$$

where, δ is the phase difference between the two light waves. This phase difference is due to both the initial phase difference between the waves, $\phi_2 - \phi_1$, and the difference in path length travelled by the waves, $s_2 - s_1$.

$$\delta = k(s_2 - s_1) + \phi_2 - \phi_1 \tag{2.1.18}$$

Looking at Eq. 2.1.17, we can see that so long as $s_2 - s_1$, ϕ_1, and ϕ_2 are independent of time, I_{12} will be non-zero and oscillate with respect to $s_2 - s_1$.

In order for the terms in I_{12} to be independent of time, the two beams must be monochromatic, with the same frequency, and have a constant phase difference [48, 50, 51]. When these conditions are satisfied, the beams are said to be mutually coherent. In reality, nothing is ever perfectly monochromatic, nor do any two sources have the same phase along the length of the beam [48]. However, these conditions can be effectively achieved by splitting and recombining a laser source, as long as this is done within the laser's coherence length [48, 50, 51].

It should also be noted that two waves do not interfere if they are polarized perpendicular to each other. In general, with randomly, or circularly polarized light, interference occurs because waves with parallel polarizations can be paired off to interfere with each other.

2.2 Diffraction Gratings

2.2.1 Constant-Pitch Diffraction Gratings

Diffraction gratings are a series of equally spaced reflecting or diffracting elements that can periodically vary the phase, amplitude, or both, of incident light [11, 48]. For example, a transmission grating with periodic transmitting grooves, in an otherwise opaque aperture, is an amplitude varying transmission grating. Some of the earliest grating constructions were of this type [11]. Conversely, a phase varying transmission grating can be a series of periodic changes in the refractive index of a material. This periodically varies the optical path length through the material, so that waves emerging from different sections have different phases [11].

A reflection grating can periodically reflect light, with each reflecting surface acting as a source of light, and the grating behaving similarly to the amplitude-varying transmission grating [11]. A reflection grating can also be a reflective surface with a periodically-varying surface profile, so that any reflected light would have a periodically varying optical path length. This grating behaves like the phase transmission grating mentioned above [11].

To illustrate how a diffraction grating affects light, Fig. 2.3 below shows an example of two rays striking two slits on a transmission grating at an arbitrary angle of incidence θ_i, and emerging at an angle θ_m. These two beams strike a similar section of the grating, separated by a single grating spacing, Λ.

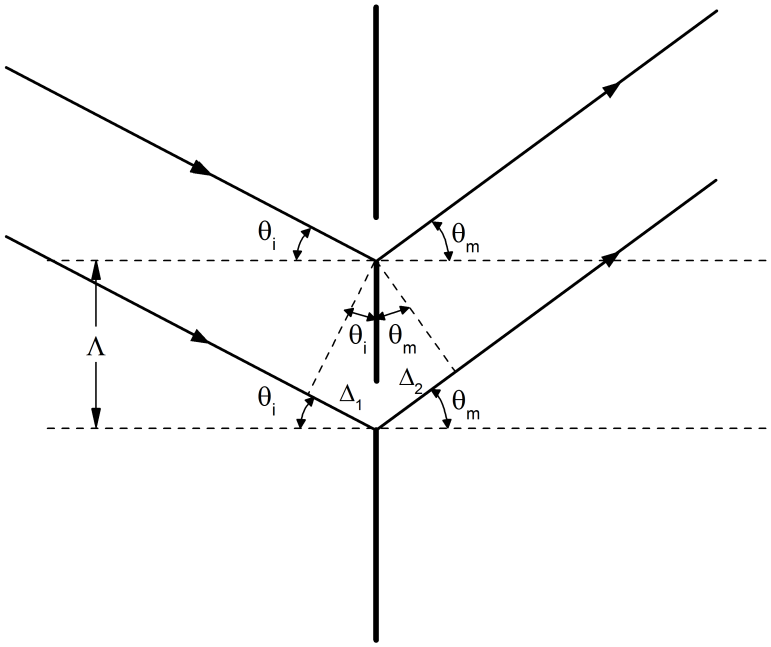

Figure 2.3: Light striking a transmission grating.

Looking at the geometry in Fig. 2.3, the net path difference between the two beams, Δ_t is

$$\begin{aligned} \Delta_t &= \Delta_1 + \Delta_2 \\ &= \Lambda \sin(\theta_i) + \Lambda \sin(\theta_m) \\ &= \Lambda \left[\sin(\theta_i) + \sin(\theta_m)\right] \end{aligned} \tag{2.2.1}$$

If the emerging beams are to interfere constructively, the path difference, Δ_t will be equal to an integer multiple of the wavelength of the incident light. This yields what is known as the grating equation, and can be applied to all types of gratings mentioned above [48].

$$m\lambda = \Lambda \left[\sin(\theta_i) + \sin(\theta_m)\right]; \quad m = 0, \pm 1, \pm 2, ... \tag{2.2.2}$$

To summarize, when monochromatic light is transmitted through, or reflected off of a diffraction grating, the resulting light interferes constructively along discrete paths, known as diffraction orders [11, 48]. These orders are labelled by an integer number m. The $m = 0^{th}$ order is the path the light would take if there was no grating structure. The angles that non-zero orders make with respect to the 0^{th} order is related to the wavelength of the light being diffracted, λ, and the spacing between the diffracting elements, Λ. This relationship is dictated by

Eq. 2.2.2. The diffracted orders are numbered as shown in Fig. 2.4. Convention dictates that positive diffraction orders are the orders that lie counter-clockwise from the 0^{th} order, while negative orders are clockwise [48]. However, this is just a convention and not required.

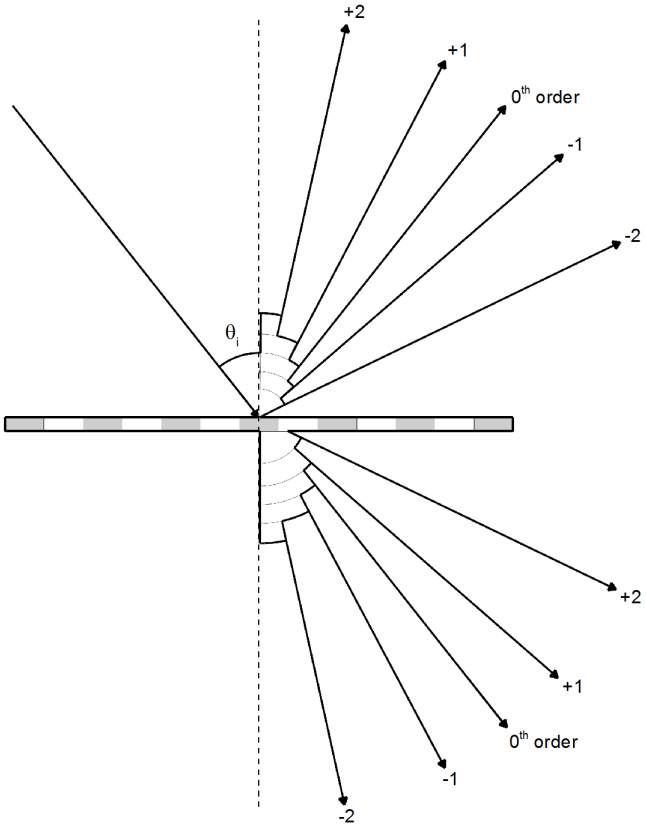

Figure 2.4: A diffraction grating and its diffracted orders.

2.2.2 Chirped-Pitch Diffraction Gratings

For a chirped diffraction grating, the spacing Λ varies over the grating in a gradual manner. If a monochromatic beam of light strikes the surface at a specific angle, say $\theta_i = 0°$, as shown in Fig. 2.5, then the grating equation becomes

$$m\lambda = \Lambda \sin(\theta_m) \tag{2.2.3}$$

We see that for a specific order m, the left-hand side of Eq. 2.2.3 is constant. Therefore, as the grating spacing increases across the chirped grating, the angle of the diffraction order must decrease. This results in asymmetrical diffraction

orders with respect to the 0^{th} order [44]. This is shown in Fig. 2.5 for the $m = \pm 1$ orders. The $m = -1$ order, located on the side with smaller grating spacings, is larger and more diffuse than the $m = +1$ order, located on the opposite side with larger grating spacings. The observation of such asymmetrical diffraction orders will be a good indication that a grating is indeed chirped.

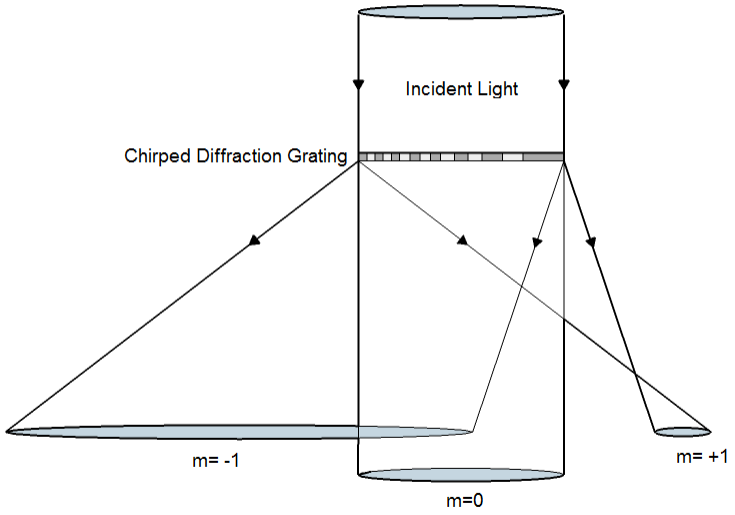

Figure 2.5: Asymmetrical diffraction orders as a result of a chirped grating.

2.3 Surface Plasmon Resonance

As mentioned before, a surface plasmon polariton is a light-induced electron density wave that occurs at the boundary between two materials where the real part of the dielectric permittivity changes sign across the interface [1]. This condition is true for a metal-dielectric interface, where the electron density wave occurs in the conduction electrons of the metal. This phenomenon is shown in Fig. 2.6-a below. The oscillating electron density in the metal couples to the incident light, binding the light to the surface [3]. This surface confinement gives rise to an electric field that is most intense at the surface and decays exponentially from the boundary between the two surfaces [1, 3], as shown in Fig. 2.6-b.

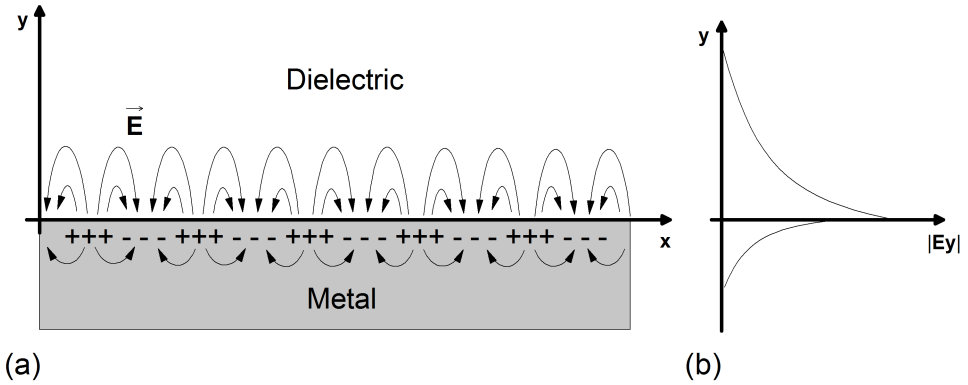

Figure 2.6: (a) A surface plasmon wave. (b) The electric field amplitude near the surface.

2.3.1 Electromagnetic Waves in a Charge-Free, Non-magnetic Material

Whenever light encounters a material, Maxwell's equations are no longer as simple as Eqs. 2.1.1 a-d, shown in Section 2.1.1. A material could contain free charges, or have a current flowing through it. In this thesis, we assume lossless dielectrics and perfect conductors. In this particular instance, Maxwell's equations can be re-written as follows [47].

$$\nabla \cdot \epsilon \vec{E} = 0 \tag{2.3.1a}$$
$$\nabla \times \vec{E} = i\omega\mu\vec{H} \tag{2.3.1b}$$
$$\nabla \cdot \mu \vec{H} = 0 \tag{2.3.1c}$$
$$\nabla \times \vec{H} = \sigma\vec{E} - i\omega\epsilon\vec{E} = -i\omega\left[\epsilon + i\frac{\sigma}{\omega}\right]\vec{E} = -i\omega\tilde{\epsilon}\vec{E} \tag{2.3.1d}$$

where,

$$\mu = \mu_r\mu_0 \tag{2.3.2}$$
$$\epsilon = \epsilon_r\epsilon_0 \tag{2.3.3}$$
$$\tilde{\epsilon} = \epsilon + i\frac{\sigma}{\omega} = \tilde{\epsilon}' + i\tilde{\epsilon}'' \tag{2.3.4}$$

Here, $\vec{H}$ is still the magnetic field strength in a material. The magnetic permeability and dielectric permittivity, μ and ϵ, are used respectively to describe a material's ability to store magnetic and electrical energy. In Eq. 2.3.2, the permeability is expressed as a product between a relative permeability, μ_r and the free-space permeability, μ_0. For a non-magnetic material, $\mu_r = 1$ [47]. Similarly,

in Eq. 2.3.3, the permittivity is expressed as a product between a relative permittivity, ϵ_r and the free-space permittivity. ϵ_0. Both are frequency dependent quantities.

Equation 2.3.4 describes what is known as the complex permittivity of a material, where $\tilde{\epsilon}' = \epsilon$ is the real part of the dielectric permittivity, and is a measure of a material's ability to store electrical energy. The imaginary part of the permittivity, $\tilde{\epsilon}''$, is a measure of how lossy, or dissipative a material is to an electric field [47, 52]. This is related to σ, the material's conductivity, as shown in Eq. 2.3.4.

Materials can be classified as lossless dielectrics, lossy dielectrics, or conductors based on their complex permittivity, and what is known as the loss tangent [52],

$$\tan(\gamma) = \frac{\sigma}{\epsilon\omega} \tag{2.3.5}$$

where, γ is the loss angle. For good conductors such as metals, $\frac{\sigma}{\epsilon\omega} >> 1$, and for poor conductors such as dielectrics $\frac{\sigma}{\epsilon\omega} << 1$.

2.3.2 Boundary Conditions

To develop the surface plasmon dispersion relation, we will start with the boundary conditions for the electric field along the surface of the metal-dielectric boundary. In Fig. 2.6-a, this boundary is located at $y = 0$. Because of the evanescent nature of the surface plasmon wave, we expect the electric field to propagate in the $\hat{x}$ direction, and decay exponentially in the $\hat{y}$ direction, as shown in Fig. 2.6-b. Therefore, if the complex fields above and below the surface are

$$y > 0 : \begin{cases} \vec{E}_d = (E_{x,d}, E_{y,d}, 0)\, e^{i(k_{x,d}x + k_{y,d}y)} \\ \vec{H}_d = (0, 0, H_{z,d})\, e^{i(k_{x,d}x + k_{y,d}y)} \end{cases} \tag{2.3.6}$$

$$y < 0 : \begin{cases} \vec{E}_m = (E_{x,m}, E_{y,m}, 0)\, e^{i(k_{x,m}x + k_{y,m}y)} \\ \vec{H}_m = (0, 0, H_{z,m})\, e^{i(k_{x,m}x + k_{y,m}y)} \end{cases} \tag{2.3.7}$$

where, the subscripts d and m represent the dielectric and metal materials, respectively. We would expect $k_{x,med}$ (wave number of medium) to have a real part, so that the wave can propagate in the $\hat{x}$ direction, and $k_{y,med}$ to be purely imaginary.

There are also general boundary conditions regarding the continuity of fields between two surfaces, as imposed by Maxwell's equations (Eqs. 2.3.1 a-d). Assuming, non-magnetic ($\mu_{r,d} = \mu_{r,m} = 1$), linear materials, these boundary conditions are [47]

$$\epsilon_d E_{y,d} = \epsilon_m E_{y,m} \tag{2.3.8a}$$

$$E_{x,d} = E_{x,m} \tag{2.3.8b}$$

$$H_{z,d} = H_{z,m} \tag{2.3.8c}$$

These conditions will be applied in the following section.

2.3.3 Applying Maxwell's Equations

To find expressions for the $k_{x,med}$ and $k_{y,med}$, Eq. 2.3.1d for the curl of the magnetic field vector $\vec{H}$ will be applied to Eqs. 2.3.6 and 2.3.7. In vector form,

$$\left(\frac{\partial H_{z,d}}{\partial y}, \frac{-\partial H_{z,d}}{\partial x}, 0\right) = -i\omega\tilde{\epsilon}_d \left(E_{x,d}, E_{y,d}, 0\right) \tag{2.3.9}$$

$$\left(\frac{\partial H_{z,m}}{\partial y}, \frac{-\partial H_{z,m}}{\partial x}, 0\right) = -i\omega\tilde{\epsilon}_m \left(E_{x,m}, E_{y,m}, 0\right) \tag{2.3.10}$$

and yields a set of four equations relating the x and y components of k, in each medium, to the frequency of the wave ω, and the amplitudes of the electric and magnetic fields.

$$ik_{y,d}H_{z,d} = -i\omega\epsilon_d E_{x,d} \tag{2.3.11a}$$

$$ik_{y,m}H_{z,m} = -i\omega\tilde{\epsilon}_m E_{x,m} \tag{2.3.11b}$$

$$-ik_{x,d}H_{z,d} = -i\omega\epsilon_d E_{y,d} \tag{2.3.11c}$$

$$-ik_{x,m}H_{z,m} = -i\omega\tilde{\epsilon}_m E_{y,m} \tag{2.3.11d}$$

Using the boundary conditions in Eq. 2.3.8a-c in Eq. 2.3.11a-d, we find

$$k_{x,d} = k_{x,m} = k_x \tag{2.3.12}$$

and

$$\frac{k_{y,d}}{k_{y,m}} = \frac{\epsilon_d}{\tilde{\epsilon}_m} \tag{2.3.13}$$

Recalling Eq. 2.1.6, for the dispersion relation of light, we know the following.

$$k^2 = \omega^2\mu\epsilon \tag{2.3.14}$$

Therefore,

$$k_d^2 = k_x^2 + k_{y,d}^2 = \omega^2\mu_d\epsilon_d \tag{2.3.15}$$

$$k_m^2 = k_x^2 + k_{y,m}^2 = \omega^2\mu_m\tilde{\epsilon}_m \tag{2.3.16}$$

Using Eq. 2.3.13 in Eqs. 2.3.15 and 2.3.16, and assuming $\mu_d = \mu_m = \mu_0$ for two non-magnetic materials, we get an expression for k_x.

$$k_x = \omega\sqrt{\frac{\mu_0\tilde{\epsilon}_m\epsilon_d}{\tilde{\epsilon}_m + \epsilon_d}} \tag{2.3.17}$$

Then, recalling Eq. 2.1.4 ($1/c = \sqrt{\epsilon_0 \mu_0}$), we can rewrite this in terms of the relative permittivities, $\epsilon_{r,med}$ and permeabilities $\mu_{r,med} = 1$ [1].

$$k_{sp} = k_x = \frac{\omega}{c}\sqrt{\frac{\epsilon_{r,d}\tilde{\epsilon}_{r,m}}{\epsilon_{r,d} + \tilde{\epsilon}_{r,m}}} = k'_x + ik''_x \tag{2.3.18}$$

Thus, k_x is a complex number where k'_x is the real part, and k''_x is the imaginary part. Substituting this expression back into Eqs. 2.3.15 and 2.3.16, we also get a complex $k_{y,d}$ and $k_{y,m}$ [1]

$$k_{y,d} = \pm\frac{\omega}{c}\sqrt{\frac{\epsilon_{r,d}^2}{\epsilon_{r,d} + \tilde{\epsilon}_{r,m}}} = k'_{y,d} + ik''_{y,d} \tag{2.3.19}$$

$$k_{y,m} = \pm\frac{\omega}{c}\sqrt{\frac{\tilde{\epsilon}_{r,m}^2}{\epsilon_{r,d} + \tilde{\epsilon}_{r,m}}} = k'_{y,m} + ik''_{y,m} \tag{2.3.20}$$

The real parts of Eqs. 2.3.18, 2.3.19, and 2.3.20 are then [15]

$$k'_{sp} = k'_x = \frac{\omega}{c}\sqrt{\frac{\epsilon_{r,d}\tilde{\epsilon}'_{r,m}}{\epsilon_{r,d} + \tilde{\epsilon}'_{r,m}}} \tag{2.3.21}$$

$$k'_{y,d} = \frac{\omega}{c}\sqrt{\frac{\epsilon_{r,d}^2}{\epsilon_{r,d} + \tilde{\epsilon}'_{r,m}}} \tag{2.3.22}$$

$$k'_{y,m} = \frac{\omega}{c}\sqrt{\frac{\tilde{\epsilon}'^2_{r,m}}{\epsilon_{r,d} + \tilde{\epsilon}'_{r,m}}} \tag{2.3.23}$$

Looking at these equations and recalling that k'_x must be real, while $k_{y,med}$, must be imaginary, we have the following conditions on the real part of the dielectric permittivity of the metal.

$$\tilde{\epsilon}'_{r,m} < 0 \tag{2.3.24a}$$

$$\tilde{\epsilon}'_{r,m} < -\epsilon_{r,d} \tag{2.3.24b}$$

2.3.4 Drude Model for Metals

The Drude model is an application of kinetic theory to the electrons in a metal. It assumes that conduction electrons are completely unbound from their host atom, and free to move around, bouncing off of the heavier and immobile positive ions [1, 49]. This classical approach gives an expression for the relative dielectric permittivity of a metal. Specifically, the real part is given as [1, 49]

$$\tilde{\epsilon}'_{r,m} = 1 - \frac{\omega_p^2\tau^2}{1 + \omega^2\tau^2} \tag{2.3.25}$$

where τ is the mean free time between electron collisions in the metal, and ω_p is known as the plasmon frequency of a metal, and is different for different metals.

For optical frequencies, $\omega\tau >> 1$, we have [1, 49]

$$\tilde{\epsilon}'_{r,m} \approx 1 - \frac{\omega_p^2}{\omega^2} \tag{2.3.26}$$

Furthermore $\omega << \omega_p$ for optical frequencies. Therefore, the $-\frac{\omega_p^2}{\omega^2}$ term will dominate, resulting in a negative real portion for the dielectric permittivity [1, 49]. Therefore, in metals, the first condition for a surface plasmon resonance wave, Eq. 2.3.24a should be satisfied.

If we substitute Eq. 2.3.26 into the second condition for surface plasmon resonance waves, Eq. 2.3.24b, we obtain a maximum for the frequency. This maximum is also known as the characteristic plasmon frequency, ω_{sp} [1, 53].

$$\omega_{max} = \omega_{sp} = \frac{\omega_p}{\sqrt{1 + \epsilon_{r,d}}} \tag{2.3.27}$$

Equation 2.3.26 is shown in Fig. 2.7 along with ω_{max}.

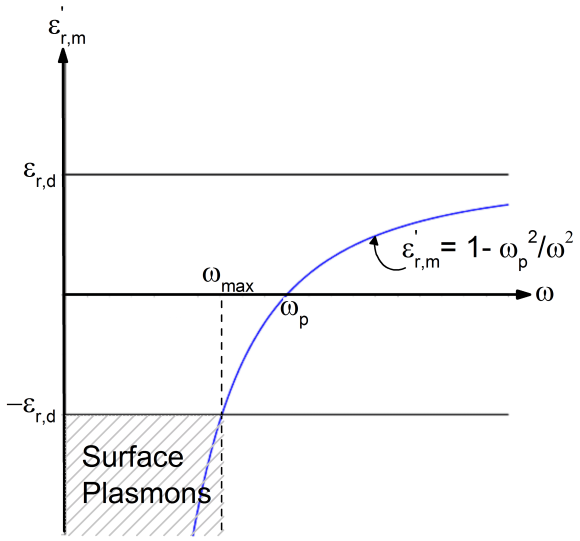

Figure 2.7: The real part of the relative permittivity of a metal as given by the Drude model.

2.4 Excitation of a Surface Plasmon

Now that the conditions for a surface plasmon to exist along a metal-dielectric interface are known, the excitation conditions will be determined. Figure 2.8 below

shows the dispersion of light in free-space, as well as the dispersion relationship for k'_x, as developed in the previous section and expressed by Eq. 2.3.21.

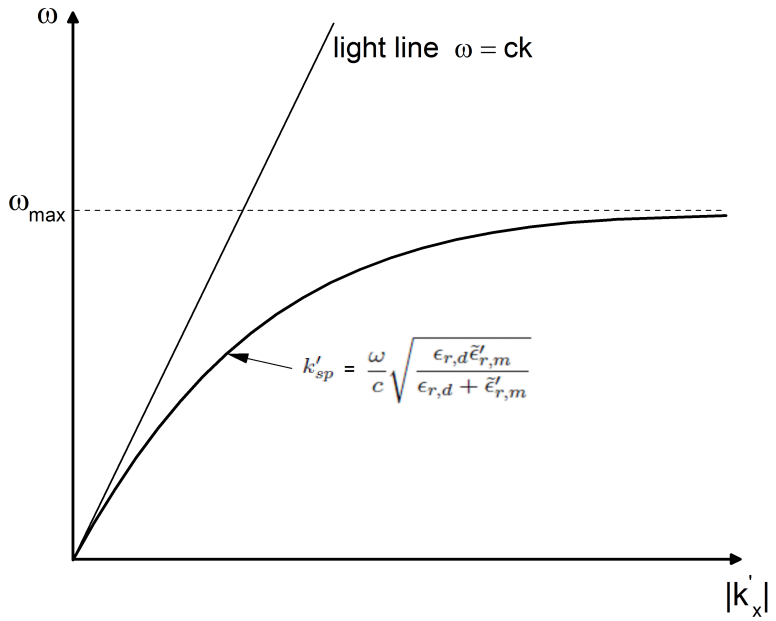

Figure 2.8: The dispersion relation for light and a surface plasmon wave.

The important thing to notice from this is that $k'_{sp} = k'_x$ never touches the light line. This can also be proven mathematically by looking at Eq. 2.3.26. When $\omega \to 0$, $\tilde{\epsilon}'_m \to -\infty$. Therefore, for small ω,

$$\lim_{\omega \to 0} \left(k'_{sp}\right) = \frac{\omega}{c}\sqrt{\epsilon_{r,d}} \tag{2.4.1}$$

Therefore, k'_{sp} will always be larger than k_{light} [1, 53]. In other words, the wavelength of the surface plasmon is always smaller than the wavelength of the incident light, preventing phase-matching along the metal surface. Therefore, the process of shining light on a flat metal surface will not generate a surface plasmon wave.

2.4.1 Excitation of Surface Plasmons Using Gratings

As mentioned in the introduction, surface plasmons can be excited by light using four principal methods. In this thesis, however, only one method, the grating method, will be used.

The main principal behind this excitation method is to increase the value of the x-component of wave-vector, $\vec{k}_{light}$, for light at the metal-dielectric interface. To understand how a grating does this, the grating equation, Eq. 2.2.2, can be rewritten in terms of the wave number $k = 2\pi/\lambda$.

$$k\sin(\theta_m) = k\sin(\theta_i) \pm \frac{2\pi m}{\Lambda} \tag{2.4.2}$$

The value $\frac{2\pi}{\Lambda}$ is the magnitude of a grating vector, K, in a direction perpendicular to the grating grooves [11]. Furthermore, as shown in Fig. 2.9, $k\sin(\theta_i)$ and $k\sin(\theta_m)$ are the vector components of the incident and diffracted light perpendicular to the grating grooves.

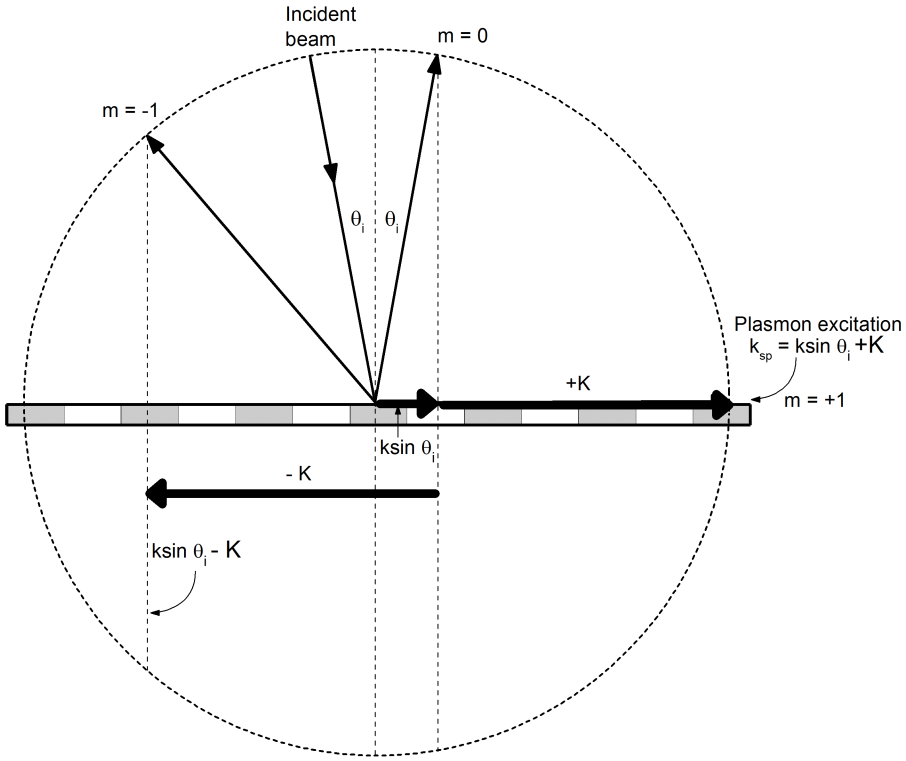

Figure 2.9: A visual representation of the grating equation in k-space.

The diffracted waves can couple to the surface plasmon if [1, 53]

$$k'_{sp} = k\sin(\theta_i) \pm \frac{2\pi m}{\Lambda}. \tag{2.4.3}$$

Therefore, for a non-zero angle of incidence, there are two solutions, a forward and backwards travelling plasmon mode. This is illustrated in Fig.2.10 for $m = 1$.

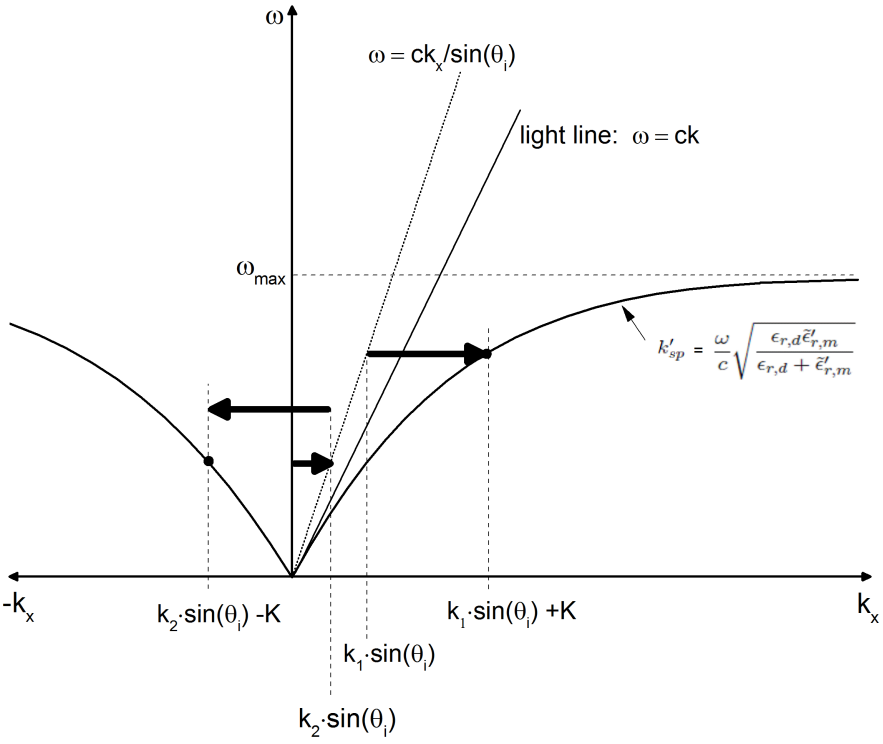

Figure 2.10: Two surface plasmon waves can be excited by a grating with a grating-vector K

By substituting Eq. 2.3.21 into Eq. 2.4.3, and using the familiar relationship between the refractive index and the permittivity, $n_d = \sqrt{\epsilon_{r,d}}$, an expression for the wavelength of incident light that will excite a surface plasmon can be found.

$$\lambda_{sp} = n_d \left(\sqrt{\frac{\tilde{\epsilon}'_{r,m}}{n_{r,d}^2 + \tilde{\epsilon}'_{r,m}}} \pm \sin(\theta_i) \right) \Lambda \tag{2.4.4}$$

Note that this equation is an approximation because it assumes that the surface plasmon will travel along a flat surface. However, for a grating, the surface will be undulating.

Also, note that in order to excite a surface plasmon wave, the electric field vector must have a component perpendicular to the grating grooves. Both vertically polarized light (TE) and horizontally polarized light (TM) can satisfy this condition, depending on the orientation of the grating.

2.5 Constant-Pitch Grating Fabrication

As mentioned in the Introduction chapter of this thesis, gratings were made by exposing an azobenzene thin film to an interference pattern at an absorbing wavelength of light.

To make a constant-pitch diffraction grating, a periodic interference pattern needs to be generated and projected onto an azobenzene sample. This is achieved with a Lloyd mirror set-up shown below in Fig. 2.11.

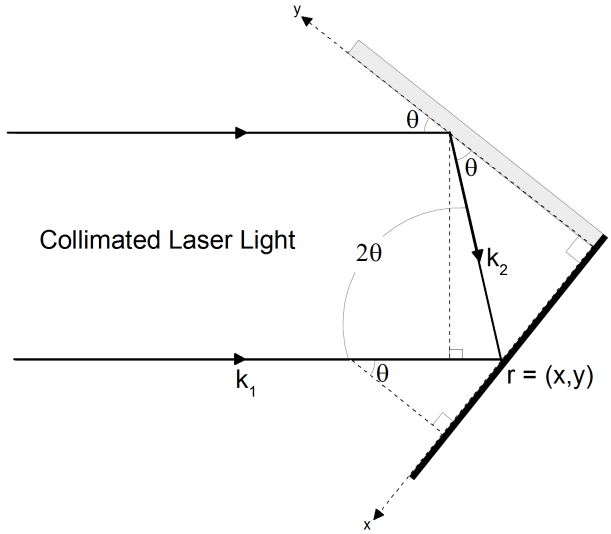

Figure 2.11: Coordinate system for the Lloyd mirror.

Half of a collimated beam of laser light strikes the sample directly, and the other half strikes a mirror placed 90° to the sample. The path-length difference between the two beams generates a phase lag between the two beam halves. As discussed in Section 2.1.3, if this is done within the coherence length of the laser, the oscillating interference term, I_{12} shown in Eq. 2.1.17, will be non-zero. As a result,

$$I \propto \cos(\delta) \tag{2.5.1}$$

where, δ is the phase difference between the two beams.

$$\delta = \vec{k}_1 \cdot \vec{r} - \vec{k}_2 \cdot \vec{r} \tag{2.5.2}$$

Here, $\vec{k}_1$ and $\vec{k}_2$ are the wave vectors of the direct and indirect laser light, respectively, at position $\vec{r}$.

Defining a two-dimensional coordinate system, shown above in Fig. 2.11 with the origin located where the mirror and sample intersect, we have the following:

$$\vec{r} = x\hat{x} + y\hat{y} \tag{2.5.3}$$

$$\vec{k}_1 = \frac{2\pi}{\lambda_{beam}}(-\sin\theta\hat{x} - \cos\theta\hat{y}) \tag{2.5.4}$$

$$\vec{k}_2 = \frac{2\pi}{\lambda_{beam}}(\sin\theta\hat{x} - \cos\theta\hat{y}) \tag{2.5.5}$$

Where λ_{beam} is the wavelength of the writing laser beam, and θ is the angle the beam makes with respect to the mirror, as shown in Fig. 2.11. $\hat{x}$ is the direction parallel to the azobenzene sample as shown in Fig. 2.11 and $\hat{y}$ is in the direction parallel to the mirror. The $\hat{z}$ direction will be ignored, since the phase difference on the sample will only depend on the orientation of the Lloyd mirror and sample in $x - y$ space.

From this, the phase difference between the two beam halves at position $\vec{r} = (x, y)$ on the film surface will be

$$\begin{aligned} \delta &= \vec{k}_1 \cdot \vec{r} - \vec{k}_2 \cdot \vec{r} && (2.5.6)\\ &= \frac{2\pi}{\lambda_{beam}}[-x\sin\theta - y\cos\theta - (x\sin\theta - y\cos\theta)] && (2.5.7)\\ &= \frac{-4\pi x\sin\theta}{\lambda_{beam}} && (2.5.8) \end{aligned}$$

Noting that when $\delta = 2\pi$, there is constructive interference, the spacing between consecutive interference maximums, Δx, can be expressed in terms of the wavelength and angle of the writing laser.

$$\Delta x = \frac{\lambda_{beam}}{2\sin\theta} \tag{2.5.9}$$

The grating spacing, Λ, is the same as the spacing between interference maxima.

$$\Lambda = \frac{\lambda_{beam}}{2\sin\theta} \tag{2.5.10}$$

2.6 Linear Chirped-Pitch Grating Fabrication

To make a chirped diffraction grating, the same Lloyd mirror set-up shown in Fig. 2.11 is used, but with a cylindrical lens placed in front of the direct half of the laser beam (see Fig. 2.12). This results in an additional phase shift, ϕ, needed to describe the phase difference between the direct and indirect beams.

$$\delta = \vec{k}_1 \cdot \vec{r} - \vec{k}_2 \cdot \vec{r} + \phi \tag{2.6.1}$$

The vectors $\vec{r}$, $\vec{k}_1$, and $\vec{k}_2$ are the same as described previously in Eqs. 2.5.3, 2.5.4, and 2.5.5 respectively. The additional phase difference is described by

$$\phi = \frac{2\pi}{\lambda_{beam}}\Delta \tag{2.6.2}$$

where Δ is the optical path difference created by the curvature of the wave front coming from the lens [54]. This is shown in detail in Fig. 2.12 below.

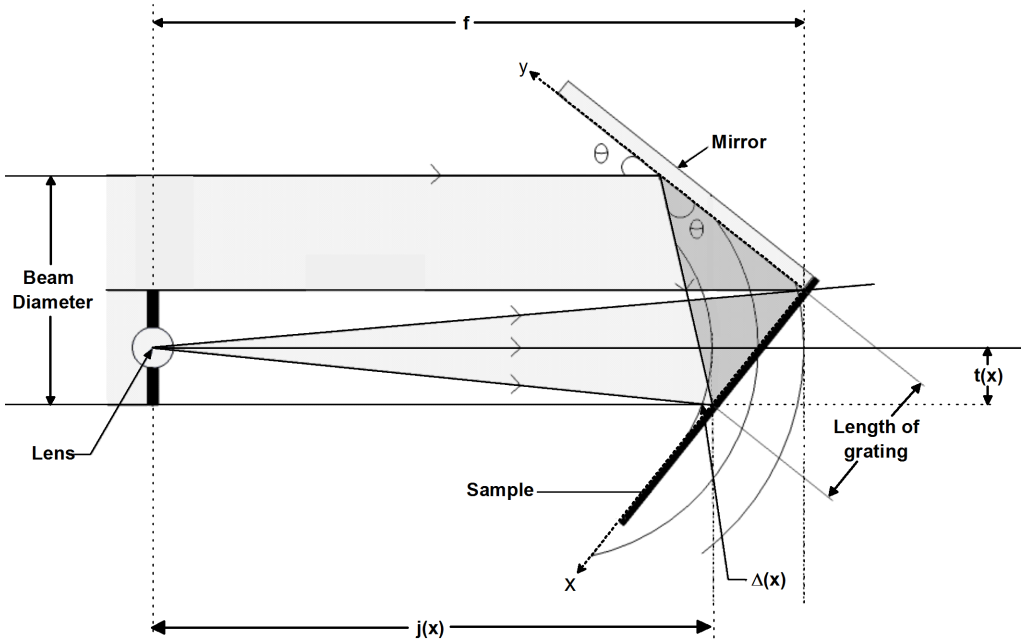

Figure 2.12: Image showing the phase difference created by the addition of a cylindrical lens in front of the direct half of the laser beam.

The equation for Δ, the path difference created by the lens, can be determined by analysing the geometry of the set-up shown in Fig. 2.12. To do this, it is easiest to first assume the lens is in the centre of the direct half of the laser beam. Then, to account for an off-centred lens, an additional term will be added after.

2.6.1 Centered Lens Geometry

For this analysis, the cylindrical lens is positioned in the center of the direct half of the laser beam, and the focal point of the lens is assumed to be in the center of the lens. From Fig. 2.12, one can see that any point directly in front of the lens will have no additional phase shift(assuming no appreciable phase lag is generated by light physically traversing the lens). For a centred lens, and a grating of length L, this location where $\Delta(x) = 0$ is at $x = L/2$ of the grating.

The length of the grating can be expressed in terms of the laser beam diameter, D, as follows:

$$L = \frac{D}{2\cos\theta} \tag{2.6.3}$$

If we define $j(x)$ to be the horizontal distance from the center of the lens to a spot on the grating, and $t(x)$ to be the vertical distance between this spot and the center of the grating, as shown in Fig. 2.12, we obtain

$$j + \Delta = \sqrt{j^2 + t^2} \tag{2.6.4}$$

From geometry, the following relations are true:

$$j(x) = f - x\sin\theta \tag{2.6.5}$$

$$t(x) = |\, x - \frac{L}{2} \,|\cos\theta \tag{2.6.6}$$

$$\begin{aligned} \Delta(x) &= \sqrt{(f - x\sin\theta)^2 + (|\, x - \frac{L}{2} \,|\cos\theta)^2} - (f - x\sin\theta) \\ &= \sqrt{(f - x\sin\theta)^2 + (|\, x - \frac{L}{2} \,|)^2\cos^2\theta} - f + x\sin\theta \end{aligned} \tag{2.6.7}$$

This gives a phase shift of

$$\delta = \frac{-4\pi x\sin\theta}{\lambda_{beam}} + \frac{2\pi}{\lambda_{beam}}\left(\sqrt{(f - x\sin\theta)^2 + (|\, x - \frac{L}{2} \,|)^2\cos^2\theta} - f + x\sin\theta\right) \tag{2.6.8}$$

where x is the x-position on the sample, ranging from 0 to L, and f is the horizontal distance from the center of the lens to the origin of the coordinate system.

2.6.2 Off-center Lens Geometry

To account for the cylindrical lens being off-center by a distance ε in the x-y plane, as seen in Fig. 2.13 below, $j(x)$ remains the same, but $t(x)$ becomes:

$$t(x) = \left| x - \left(\frac{L}{2} + \frac{\varepsilon}{\cos\theta}\right)\right| \cos\theta \tag{2.6.9}$$

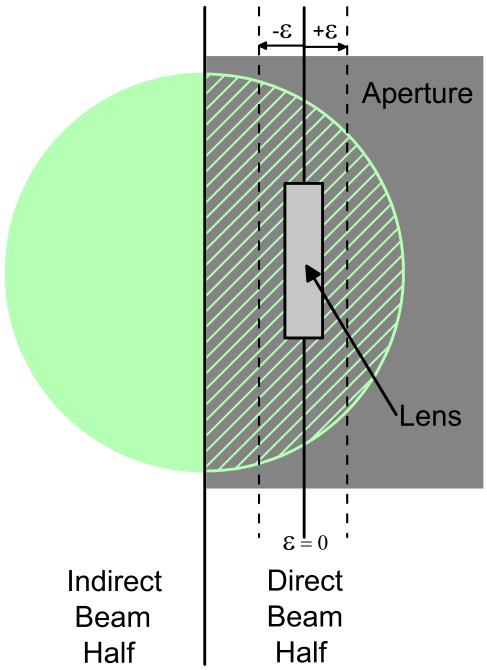

Figure 2.13: Image depicting lens placement with respect to the writing laser beam.

Here, a positive ε is a horizontal offset towards the outside of the laser beam, and a negative ε is a horizontal offset towards the center of the beam. This gives an optical path length of

$$\begin{aligned}\Delta(x) = &\sqrt{(f - x\sin\theta)^2 + \left(\left|x - \left(\frac{L}{2} + \frac{\varepsilon}{\cos\theta}\right)\right|\cos\theta\right)^2} - (f - x\sin\theta) \\ = &\sqrt{(f - x\sin\theta)^2 + \left(x - \left(\frac{L}{2} + \frac{\varepsilon}{\cos\theta}\right)\right)^2\cos^2\theta} - (f - x\sin\theta)\end{aligned} \tag{2.6.10}$$

The resulting phase shift between the light from the cylindrical lens and the light hitting the mirror is then

$$\delta = \frac{-4\pi x\sin\theta}{\lambda_{beam}} + \frac{2\pi}{\lambda_{beam}}\left(\sqrt{(f - x\sin\theta)^2 + \left(x - \left(\frac{L}{2} + \frac{\varepsilon}{\cos\theta}\right)\right)^2\cos^2\theta} - (f - x\sin\theta)\right) \tag{2.6.11}$$

Using Eq.2.6.11 in Eq.2.5.1, the irradiance profile can be plotted for different angles θ of the sample and mirror, as well as for different positions x along the grating. The grating length, L, can also be varied and is dictated by the aperture diameter, D, of the collimated laser beam and the angle, θ, it makes with the

Lloyd mirror set-up. Additionally, different lens positions as described by f and ϵ can be analysed, to see how this effects the chirping of the grating.

Figure 2.14 plots the expected grating pitch at five areas along the length of different chirped-pitch diffraction gratings, all with the same $\varepsilon = 0.0$ mm and $f = 69$ mm values. Looking at this plot, the grating pitch does not vary in a perfectly linear manner across the chirped-pitch gratings, but instead the chirping rate increases slightly across the grating. The inset of Fig. 2.14 shows what a typical chirped-pitch grating will look like, with the expected horizontal length shown. The gratings are semi-circle in shape, due to the circular shape of the laser in the grating fabrication set-up. The flat side of the grating corresponds to the side closest to the mirror during grating fabrication.

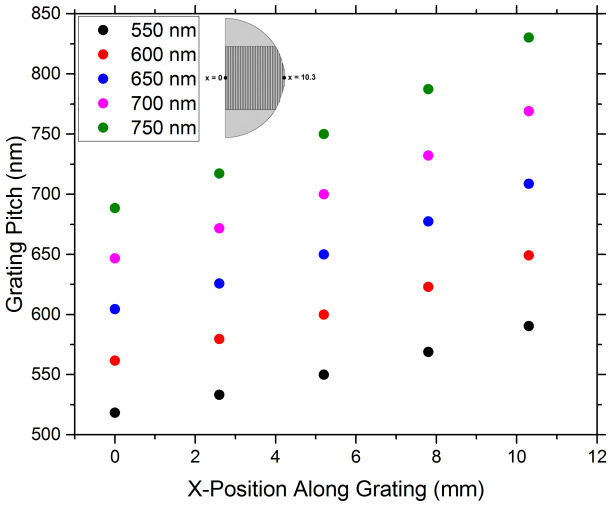

Figure 2.14: The grating pitch across five different chirped-pitch gratings. All gratings are assumed to have an f-value of 69 mm, and an ε-value of 0.0 mm. The inset shows an example of a chirped-pitch grating and its expected length.

Figure 2.15 gives the theoretical grating pitches at opposite sides of chirped-pitch diffraction gratings as the distance between the cylindrical lens and azobenzene sample, f, varies.

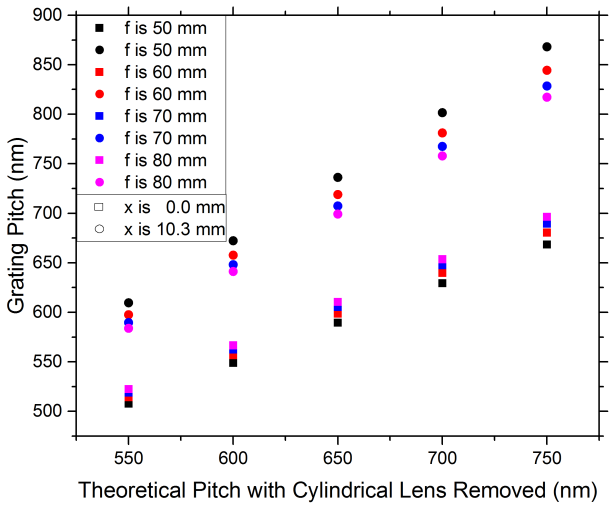

Figure 2.15: The grating pitches at opposite sides of different chirped-pitch diffraction gratings made with the cylindrical lens placed at different distances, f, from the azobenzene sample during grating fabrication.

As one would expect, when f increases, the radius of curvature of the light from the lens is larger at the azobenzene sample surface. In other words, the wavefront becomes increasingly flat, as the cylindrical lens is moved further away from the azobenzene sample, resulting in less chirping in the subsequently produced grating.

Figures 2.16, 2.17, and 2.18 demonstrate what is expected to happen to the pitches of a chirped-pitch diffraction grating if the horizontal position of the lens, ε, with respect to the writing laser beam profile (Fig. 2.13), is changed.

Specifically, Fig. 2.16 is a plot of the theoretical pitch of the flat side of the diffraction grating, at the $x = 0$ mm position (as shown on the inset of Fig. 2.14), as ε changes.

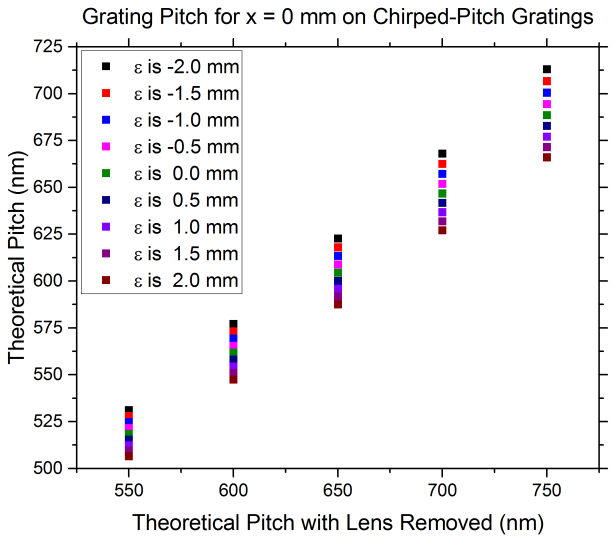

Figure 2.16: The smallest theoretical pitch for chirped-pitch diffraction gratings made with different horizontal offsets, ε, of the cylindrical lens during grating fabrication.

Figure 2.17 on the other hand is a plot of expected grating pitch on the curved side of the grating, or the $x = 10.3$ mm position on a 10.3 mm wide grating.

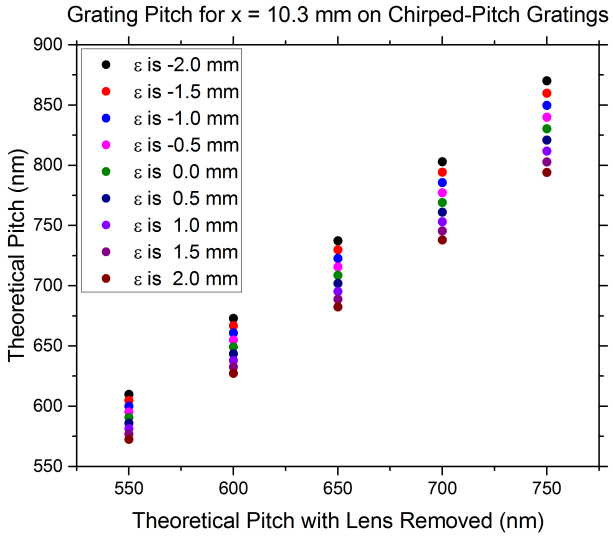

Figure 2.17: The theoretical largest pitch for chirped-pitch diffraction gratings made with different horizontal offsets, ε, of the cylindrical lens during grating fabrication.

Finally, Fig. 2.18 is a plot of the expected chirping rate of different gratings made with different ε values. It is defined as the change in grating pitch, divided by the length of the diffraction grating. This chirping rate assumes a constant rate of change in the grating pitch, which from Fig. 2.14 is not quite the case, so this calculated rate is only an average rate across the entire grating.

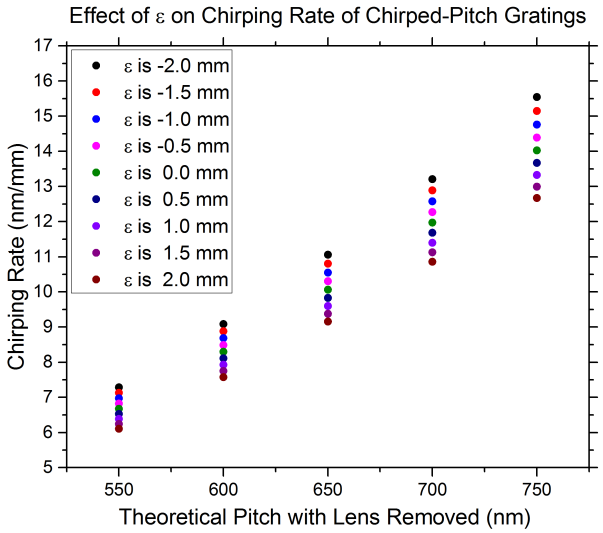

Figure 2.18: The theoretical grating pitch at different areas along different chirped-pitch gratings.

From Figs. 2.16, 2.17 and 2.18, it can be concluded that the horizontal movement of the cylindrical lens with respect to the beam profile has a significant effect on both the central pitch of the grating and the average rate of chirping across the grating. Specifically, a larger range in pitch and chirping rate is expected if the cylindrical lens is placed closer to the center of the writing laser, with a negative ε value.

3 Experimental Procedure and Optimization

This chapter will outline the experimental procedure and equipment used to obtain the results in this thesis. This includes details about the azobenzene sample preparation, gratings fabrication, and how spectral measurements were carried out, as well as some of the optimization steps required to get the best surface plasmon signal.

3.1 Azobenzene Sample Preparation

To make a diffraction grating, an azobenzene thin film must first be deposited onto a transparent substrate. In this thesis, the substrates were Corning 0215 soda lime glass microscope slides with dimensions of 38 $\times$ 38 mm^2 and 1 mm thickness. Before their use, these slides were cleaned with dish soap and water to remove any dirt and oil on their surface. Then, the slides were dried with lint-free Kimwipes and placed in a Yamato oven at 95 °C for 30 minutes to evaporate any remaining water.

Before the azobenzene solution was deposited onto the substrates, the glass slides were blown dry one last time with clean and compressed air to remove any settled dust. These steps were necessary to ensure an even thin film could be deposited across the glass.

Once clean, approximately 3 mL of a solution, containing Disperse Red 1 azobenzene molecular glass and dichloromethane, at a 3 wt% mix ratio, was deposited on each slide. These slides were then spun at 1100 rpm for 20 seconds, using a Headway Research spin-coater and then placed back into a Yamato oven, at 95 °C, for another 30 minutes to evaporate the remaining solvent.

The thickness of the remaining azobenzene film was measured using a Dektak IID profilometer. Measurements were taken from multiple samples, and from multiple areas on each sample, i.e. the center of the sample, and the edges of the sample, to ensure the azobenzene film was approximately uniform. The average

film thickness was measured to be (240±30) nm, where the uncertainty it just half of the the difference between the maximum and minimum thickness measured.

3.2 Grating Inscription on Azobenzene Thin Films

Two different experimental set-ups were used to fabricate constant-pitched gratings and chirped-pitch gratings.

3.2.1 Constant-Pitched Gratings

As mentioned in previous chapters, if a constant-pitch interference pattern is shone onto an azobenzene thin film, the interference pattern will photo-mechanically imprint onto the surface of the film, creating a constant pitch, and sinusoidal surface relief grating.

To generate a constant-pitch interference pattern, a Lloyd mirror set-up, like the one shown in Fig. 3.1, was used.

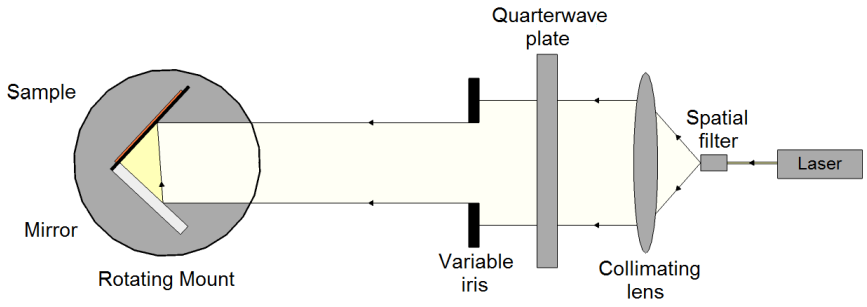

Figure 3.1: Experimental set-up used to make a constant-pitched grating.

A Coherent Verdi diode-pumped laser with a wavelength of 532 nm was passed through a spatial filter and then collimated with a lens. A quarter-wave plate was used to generate circularly polarized light. This was necessary to assure that azobenzene molecules of any orientation within the thin film [55] would be able to undergo the cis-trans isomerisation mentioned in the introductory chapter of this thesis.

Finally, this light would pass through a variable iris before being incident on the Lloyd mirror configuration. The irradiance of the beam at this point was 312 mW/cm^2, as measured using a Coherent Power-Max sensor. This was found to be the highest irradiance possible, without causing abnormal changes in the grating

depth along the surface of the grating. A lower irradiance would take longer to generate a grating with the same groove depth. This will be shown explicitly in the Results chapter of the thesis.

The Lloyd mirror configuration consisted of a mirror placed 90° to an azobenzene sample, as shown in Fig. 3.1. Half of the incoming light was made incident upon the sample directly, while the other half would reflect off the mirror before being incident on the same area of the sample. As discussed in the Theory chapter of this thesis, this would generate a constant-pitch interference pattern on the sample surface. The pitch of this interference pattern, and therefore the pitch of the grating, was controlled by the angle of the Lloyd mirror configuration with respect to the incoming beam. The depth of the grating was also controlled by the exposure time. Finally, the size of the grating could be controlled by the size of the variable iris aperture.

For constant-pitch gratings, the laser exposure time was set between 10 and 30 seconds, with an aperture diameter typically, between 9 and 10 mm. This fabrication process would result in small, semi-circular diffraction gratings, as shown below in Fig. 3.2. Note that the horizontal width of the diffraction grating in Fig. 3.2 is not simply the radius of the aperture used, but is governed by Eqn. 2.6.3 from Section 2.6.1 of the Theory chapter of this thesis. Gratings with pitches ranging from 550 nm to 800 nm, made with an aperture opening of 9.5 mm, would make gratings with a vertical dimension of 9.5 mm and a horizontal dimension ranging from 5.0 mm to 5.4 mm.

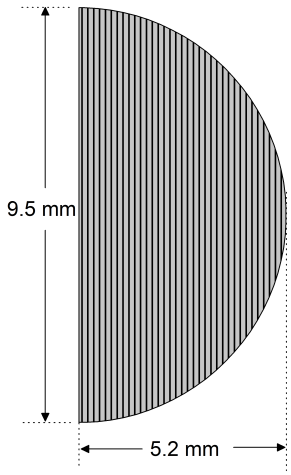

Figure 3.2: A not-to-scale representation of a constant-pitch diffraction grating.

3.2.2 Chirped-Pitch Gratings

To make the chirped-pitch gratings, the same laser and Lloyd mirror set-up for constant-pitch gratings was used, but with a cylindrical lens placed in the direct half of the laser beam, as shown in Fig. 3.3.

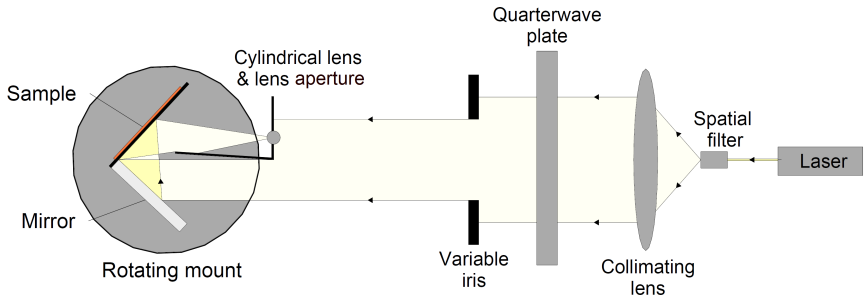

Figure 3.3: Experimental set-up used to make chirped-pitch gratings.

As discussed in Section 2.4.1, the cylindrical lens curves the wave-front of the direct half of the laser beam. This creates an additional phase lag between the direct and indirect beam halves giving rise to a chirped interference pattern on the surface of the film. This in turn will generate a chirped-pitch grating.

To make sure only the light from the cylindrical lens reached the sample, the lens was placed in a custom cardboard, rectangular aperture. Furthermore, an additional piece of thin cardboard was placed $\approx 80°$ to the lens aperture, as shown in Fig. 3.3, to prevent stray light from hitting the mirror and creating additional interference on the sample surface. Without this light blocker, the additional interference was enough to generate additional grooves on the grating. This was made apparent when the gratings were illuminated with a 632.8 nm Helium-Neon laser during the measurement of their grating spacing (procedure described below in Section 3.3). Additional and slightly asymmetrical diffraction orders, with respect to the 0^{th} order, were visible from gratings made without the light-blocker. With the light blocker in place during the grating fabrication, these additional diffraction orders disappeared.

Furthermore, to ensure that the vertical axis of the lens was not tilted with respect to the Lloyd mirror set-up, the beam of light emerging from the cylindrical lens, perpendicular to the axis of the lens, was aligned on a wall behind the set-up, a distance of 2 m away, with the reflected beam-half coming from the Lloyd mirror. Again, if this was not done properly, there would be visible irregularities in the diffraction pattern produced by illuminating the gratings with a 632.8 nm Helium-Neon laser. In this case, there were no additional diffraction orders, but

instead the expected diffraction orders were skewed in appearance. This would subsequently, affect the spectra obtained from the gratings.

For this thesis, a cylindrical lens of diameter (4.0 ± 0.1) mm was chosen and embedded in a custom cardboard aperture with dimensions 4×7 mm^2. To ensure the entire lens aperture was illuminated, the variable circular aperture in Fig. 3.3 was opened to (18.9 ± 0.1) mm. In addition, the distance between the lens and the sample was chosen to be (69 ± 1) mm. This would produce gratings with the approximate dimensions shown below in Fig. 3.4. Again, it should be noted that the horizontal length of the grating, shown as 10.3 mm in Fig. 3.4, will vary somewhat, depending on the angle θ in Eq. 2.6.3. For chirped gratings with a central pitch ranging from 600 nm to 750 nm, the width is expected to vary from 10.1 mm to 10.5 mm. Also note that with the cylindrical lens and custom aperture in place, the intensity of the direct beam will be considerably less than in the constant-pitch grating fabrication set-up. As a result, longer exposure times are expected for chirped-pitch gratings.

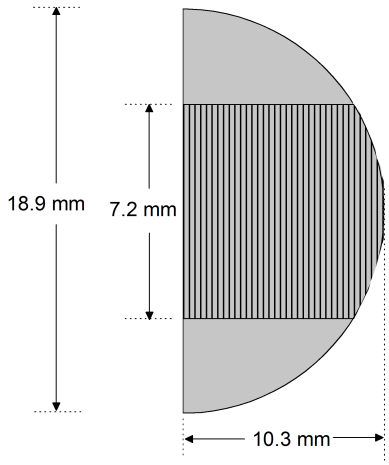

Figure 3.4: A chirped-pitch diffraction grating.

Once the azobenzene gratings were fabricated, they were coated with a layer of silver, 60 nm thick, using a Bal-Tec SCD-050 sputter coater. The silver layer takes the shape of the underlying azobenzene grating [34] as depicted in Fig. 3.5 and allows surface plasmon excitation to occur at the silver-air interface.

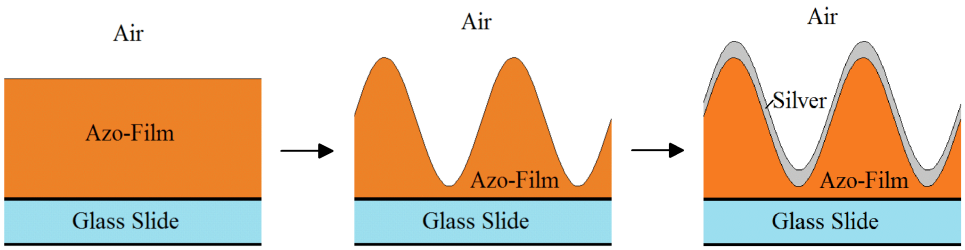

Figure 3.5: Fabricaton steps in making a sinusoidal, metallic, surface-relief grating.

Figure 3.6 below gives an example image of six different chirped-pitch diffraction gratings fabricated on the same glass slide after they have been coated in a 60 nm layer of silver.

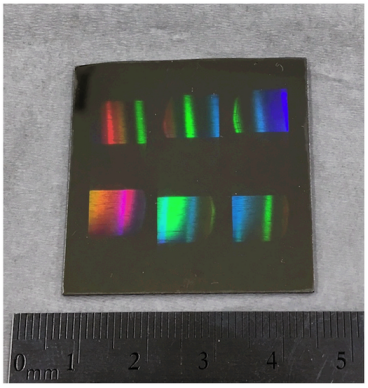

Figure 3.6: A photograph of six different chirped-pitch diffraction gratings after they have been coated with silver.

3.3 Measuring the Pitch of Diffraction Gratings

To measure the pitch of the fabricated diffraction gratings, the set-up shown in Fig. 3.7 was used along with the grating equation, familiar from the Theory chapter of this thesis.

$$m\lambda = d\,(\sin\alpha \pm \sin\beta) \tag{3.3.1}$$

Here, λ is the wavelength of probing light, 632.8 nm from a Helium-Neon laser, d is the grating spacing, m is the integer diffraction order, and α and β are the incident and diffracted angles, respectively.

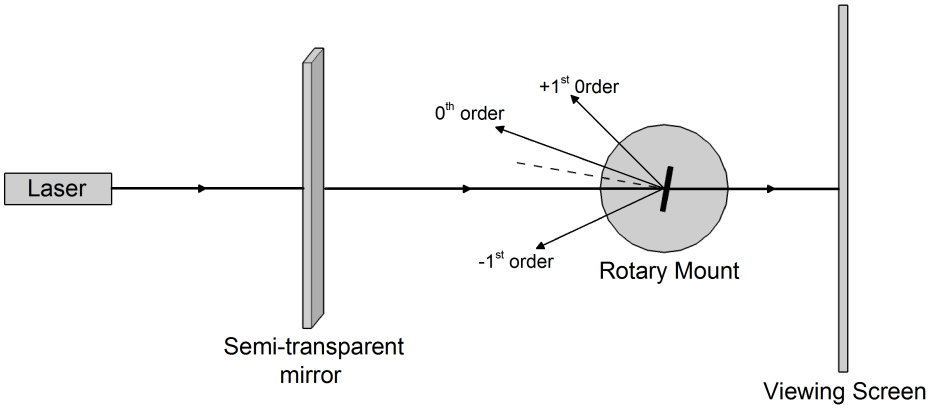

Figure 3.7: Apparatus used to measure the grating pitch.

To measure the grating spacing, d, light from the Helium-Neon laser was shone through a semi-transparent mirror, before hitting the grating. This mirror was tilted, so that light reflected off the grating and back at the mirror, was reflected upwards onto a viewing screen behind the sample.

With a grating placed atop a motorized rotating table, the angles of the 0^{th}, $+1^{st}$ and -1^{st} diffraction orders could be measured. Using these angles and equation 3.3.1, two separate measurements for the grating spacing could be obtained and averaged.

3.4 Spectral Analysis

As discussed in Section 2.4.1, when light is shone onto a metallic diffraction grating, a surface plasmon polariton wave will be excited if the light is of the correct wavelength, angle, and polarization. What has not been discussed is how SPP waves affect the transmission and reflection spectra of metallic diffraction gratings.

Light that is coupled into a surface plasmon along the metal-dielectric interface of a diffraction grating can travel along the surface until its energy is dissipated as heat, or until it decouples back into light. Any decoupled light that is re-emitted in the direction of specularly reflected light will deconstructively interfere with the specularly reflected light [56]. This is because light that is specularly reflected off a metallic surface will undergo a 180° phase shift [47]. However, the de-coupled surface plasmon light will not undergo this phase shift, making the two light sources 180° out of phase. This results in a dip in the reflection spectrum at the SPP excitation wavelength, λ_{SP}, from deconstructive interference. The energy loss in the reflected beam is transferred to the transmitted beam and is seen as a peak in transmission at the SPP excitation wavelength [56].

For all spectroscopic measurements, the gratings were positioned with their grating vector aligned horizontally. This means horizontally polarized light (TM-polarized) was expected to excite a surface plasmon resonance wave. To help isolate the surface plasmon signal, all transmission and reflection spectra were TM/TE normalized. In other words, the separate spectra obtained under TM polarization (horizontally polarized light) was divided by the spectra obtained under TE polarization (vertically polarized light). If no polarization dependent phenomena, like SPP waves were present, then the normalized spectra would be a straight line located at TM/TE =1.

3.4.1 Scanning Spectrometer: Reflection

Spectroscopic measurements in reflection were made using the apparatus shown below in Fig. 3.8. A monochromator cycled through different wavelengths ranging from 400 nm to 900 nm, while a photo-detector measured the intensity of the reflected light coming from the grating at individual wavelengths.

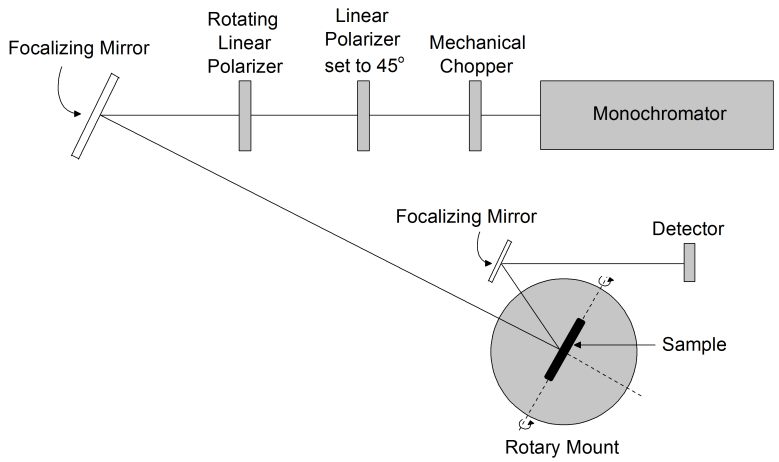

Figure 3.8: Apparatus used to make spectroscopic measurements in reflection.

The light from the monochromator was first mechanically chopped and sent through a linear polarizer set at 45°, followed by a rotating linear polarizer, so that both TE polarized light and TM polarized light could be produced. This light reflected off of a concave mirror and focalized onto the sample. In order to measure the reflected spectra, the sample was tilted upwards slightly to allow reflected light to reach another, smaller, concave mirror, situated above the incoming incident light (this is shown beside the incident light in Fig. 3.8). Because of the horizontal orientation of the grating vector, this upwards tilt did not affect the surface plasmon excitation wavelength, and the angle of incidence was still 0° with respect to the vertical grating grooves.

The light from the second focalizing mirror was then directed at a photo-detector, which was connected to a lock-in amplifier. Using the lock-in amplifier and the mechanical chopper, the detection of background light was minimized.

Also note that the sample was positioned on a rotational mount. This allowed for additional spectra to be taken at non-zero angles of incidence.

3.4.2 Scanning Spectrometer: Transmission

Transmission measurements of a diffraction grating were also made with the same set-up as before, but with the photo-detector positioned directly behind the sample, as seen in Fig. 3.9.

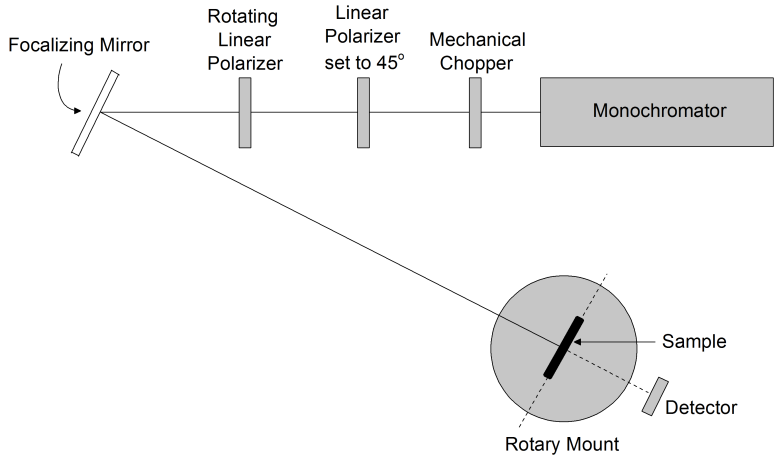

Figure 3.9: Apparatus used to make spectroscopic measurements in transmission.

Again, the spectrometer could cycle between wavelengths ranging from 400 nm to 900 nm, taking individual transmission measurements from a small portion of the full 400-900 nm spectrum at a time. For this reason, this set-up was not capable of explicitly showing simultaneous excitation of a broad-band of surface plasmon resonance waves from a single diffraction grating. To do this, a different spectrometer set-up was used and is described in the following section.

3.4.3 Fiber Spectrometer Transmission Over an Entire Diffraction Grating

Two additional set-ups were used to obtain either the transmission from an entire diffraction grating, or from a small area on a diffraction grating across the entire visible spectrum at once.

Figure 3.10 below provides a visual of the apparatus used to measure the transmission spectrum from an entire diffraction grating. The light from an Oriel

Corp. halogen lamp was passed through a neutral density filter to control the final relative light intensity. The light was then passed through a linear polarizer, adjustable to produce either vertically polarized light (TE), or horizontally polarized light (TM). Then, before illuminating the sample at a 0° angle of incidence, the light was incident on a rectangular aperture, producing a rectangular beam of light large enough to span an entire grating. This was especially useful for obtaining the spectra from chirped-pitch diffraction gratings, which were approximately rectangular in shape. If a circular aperture was used on these gratings instead, it would have produced a larger surface plasmon signal for grating spacings located in the center of a circular beam. Since this thesis attempts to show a uniform band of surface plasmon excitation intensity, a rectangular aperture was chosen.

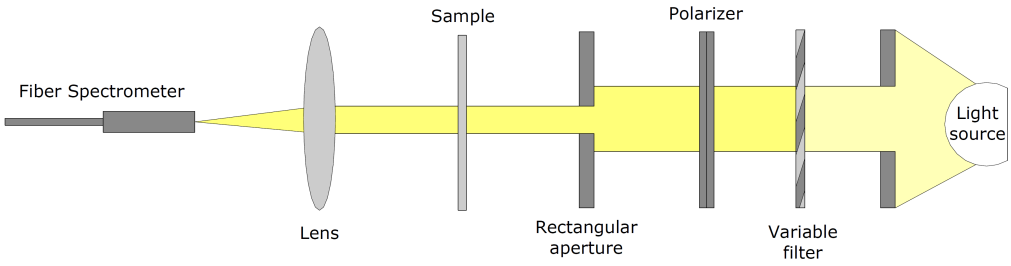

Figure 3.10: Apparatus used to make transmission measurements across the entire area of a diffraction grating.

After illuminating a grating, the transmitted light was focused into an Edmund optics CCD fiber optic spectrometer using a focalizing lens. Though the halogen lamp produced light according to a black body radiation curve, the silicon detector inside of the CCD spectrometer could only detect wavelengths within a range of 400 nm to 900 nm. For this reason, gratings with spacings that produce SPP wavelengths within the range of 500 nm to 800 nm were fabricated and used throughout this thesis. Also, for each spectral measurement, an integration time of 100 ms was used, and from visual inspection of the spectra, that gave an adequate signal to noise ratio.

3.4.4 Fiber Spectrometer Transmission Over a Small Area of a Diffraction Grating

To obtain the transmission spectrum from a specific area on a grating, the same set-up described above was used, but with an additional focalizing lens placed between the polarizer and the sample, as shown below in Fig. 3.11. This lens was used to focus the light down to a spot-size of approximately 1 mm in diameter.

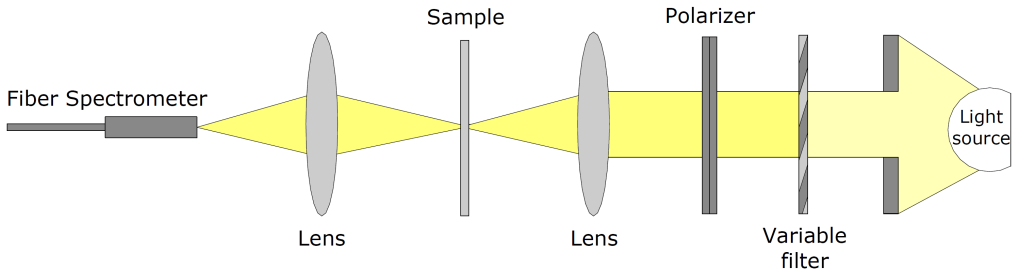

Figure 3.11: Apparatus used to make spectroscopic measurements in transmission from a small 1 mm diameter area on a grating.

By taking TM/TE normalized transmission measurements from different areas on a diffraction grating, one could observe possible changes in the grating depth and grating pitch across a single grating.

4 Results and Discussion

In this chapter, data obtained using the apparatus and procedures outlined in Chapter 3 will be presented and discussed. The goal was to compare the surface plasmon excitation from chirped-pitch gratings with that of constant-pitch gratings. However, before this could be done, the surface plasmon signal from both types of gratings had to be identified and optimized by adjusting various grating parameters like depth, silver layer thickness, and excitation wavelength. The goal of this optimization was to produce the highest surface plasmon peak with as little additional phenomenon visible in the spectra as possible.

Since spectroscopic measurements were done for wavelengths ranging from 400 nm to 900 nm, gratings that excite surface plasmons within this wavelength range were desirable.

Recalling Eq. 2.4.4 from Section 2.4.1, the grating pitch, Λ, necessary to excite a surface plasmon at a specific wavelength, λ_{SP}, can be calculated if the dielectric permittivity of the metal and dielectric material are known. Using available permittivity data for silver [57] and air [58], the theoretical plot shown in Fig. 4.1 was made. This plot relates the grating pitch to the wavelength of the surface plasmon wave, assuming the incident light is normal to the grating.

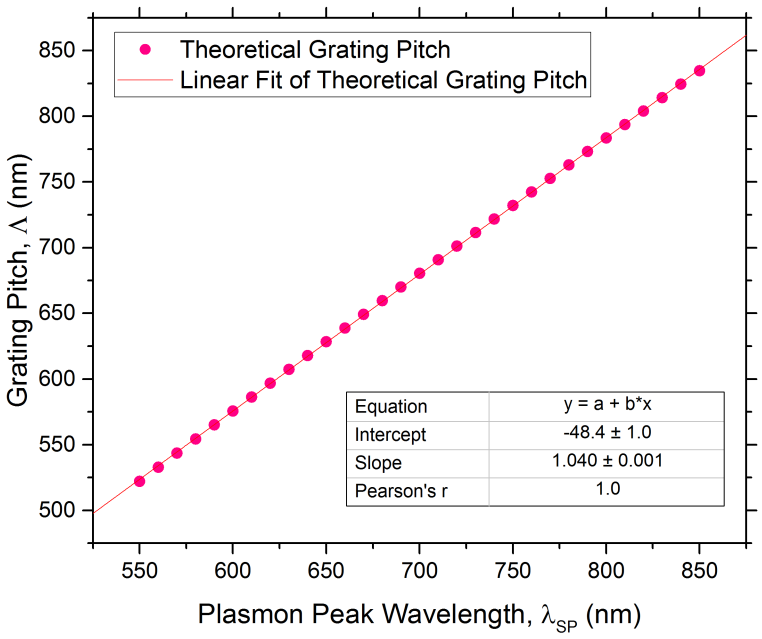

Figure 4.1: The grating pitch, Λ, that will theoretically couple light with a normal angle of incidence and free-space wavelength, λ_{SP}, into a surface plasmon polariton at a silver-air interface.

Figure 4.1 shows that for optical wavelengths, the grating pitch (nm) is linearly proportional to the surface plasmon wavelength (nm). From the plot, the following relationship is obtained.

$$\Lambda = 1.04\,(\lambda_{SP}) - 48.4 \tag{4.0.1}$$

Therefore, if the incident light has wavelengths ranging from 550 nm to 850 nm, gratings with spacings from 500 nm to 850 nm should be able to excite surface plasmon polaritons.

Knowing what grating pitches were needed, the next step was to make sure the laser-writing set-up described in Section 3.2.1 was generating the correct grating pitches. This was done by varying the angle of the Lloyd mirror set-up with respect to the incoming laser light. As dictated by Eq. 2.5.10 in Section 2.5 of the chapter on Theory, this would give rise to different grating pitches. These pitches could then be measured using the HeNe laser set-up described in Section 3.3 of the Procedure. The result of this is given below in Fig. 4.2, and shows good agreement between the expected and measured grating pitches. Note however,

the rotating Lloyd mirror set-up was prone to movement over time with repeated sample placements, so this set-up had to be checked regularly.

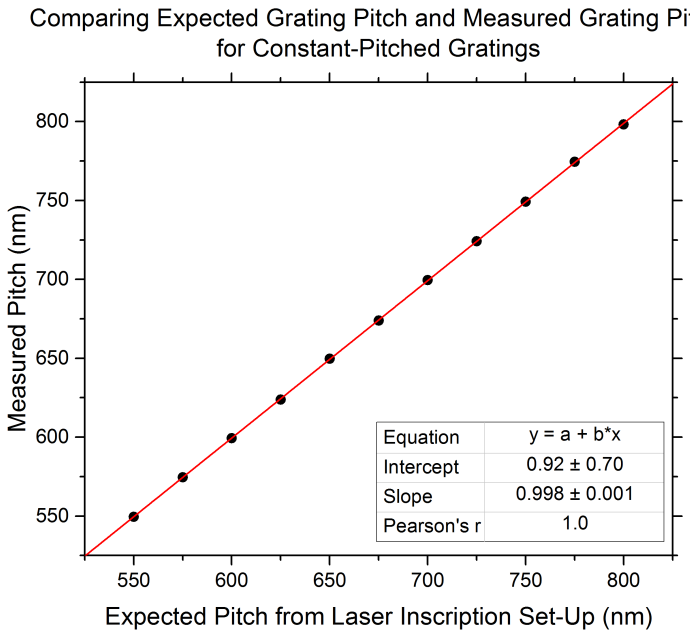

Figure 4.2: A plot comparing the expected and measured grating pitches from the grating fabrication set-up.

4.1 Optimization of Constant-Pitched Diffraction Gratings

Once gratings of a desired pitch could be made, a number of steps were taken to produce a strong and distinguishable surface plasmon resonance peak in transmission.

4.1.1 Optical Laser Irradiance

The first parameter that was optimized was the writing laser's irradiance, which was dictated by the output power of the writing laser. A higher irradiance during the azobenzene exposure resulted in a grating with an increased surface profile depth in a shorter exposure time.

Figure 4.3, shown below, presents the transmission spectra obtained from different areas of a grating for four different gratings. Each grating was made using the laser writing set-up detailed in Section 3.2.1, with an exposure time

of 400 seconds, grating pitch of 650 nm, but with different laser irradiances, as represented by the laser's output power. Each grating was subsequently coated with 70 nm of silver.

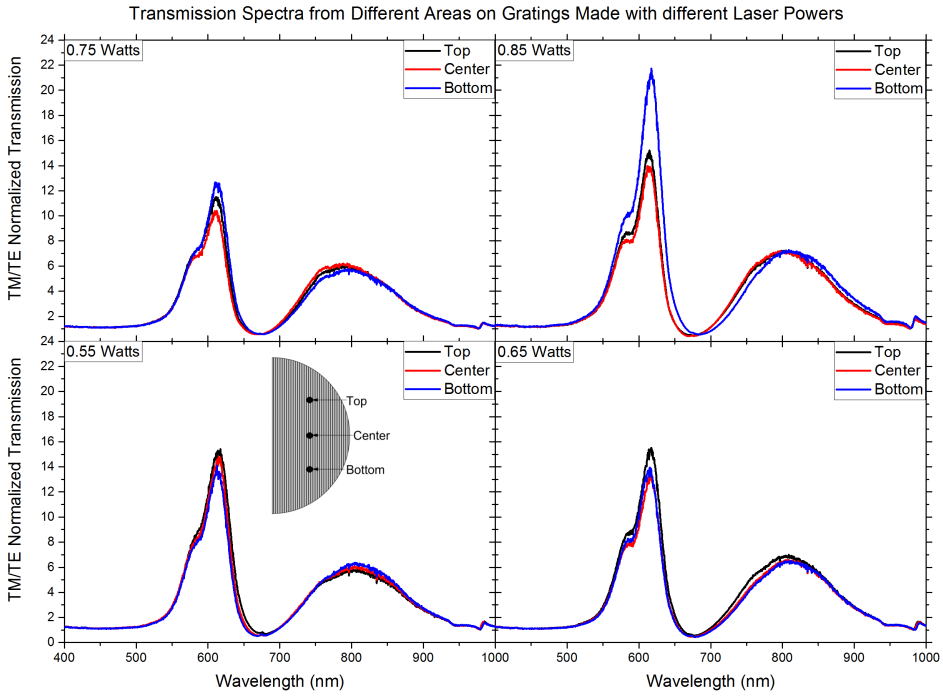

Figure 4.3: Four plots from four gratings made with the inscribing laser at different power settings. Each plot shows the trasnsmission from different areas on the gratings. All gratings were made with an exposure time of 400s, a pitch of 650 nm, and were coated with 70 nm of silver.

From the height of the transmission peaks in Fig. 4.3, it can be seen that the transmission is non-uniform across all of the gratings. This could be due to a number of things including non-uniform azobenzene thickness, non-uniform silver thickness, or non-uniform laser irradiance during grating fabrication. When the laser power is increased to 0.85 Watts, the transmission becomes even more non-uniform, with one area of the grating transmitting roughly 1.5 times more TM/TE normalized light than the other two areas. In addition, gratings that were fabricated with a writing laser power of 0.85 Watts and higher, looked visibly different than those made on a lower laser power setting. Specifically, a circularly shaped, smooth area would appear on gratings made with a high laser power. For this reason, all subsequent gratings were made with the laser set to 0.75 Watts, the highest irradiance possible without damaging the grating. This output power

produced an average irradiance measured to be 312 mW/cm^2.

It should also be noted that the transmission spectra shown in Fig. 4.3 do not show a transmission peak at the expected plasmon wavelength of 671.5 nm for a 650 nm grating pitch. Further optimization, discussed in the following section, revealed that much shorter exposure times were required.

4.1.2 Laser Writing Time

The second parameter optimized was the exposure time of the azobenzene sample to the interfering laser light. The longer the exposure time, the greater the depth of the grating.

Figure 4.4 below depicts the TM/TE normalized transmission spectra obtained from gratings with a 650 nm spacing, all made with the same irradiance (312 mW/cm^2), but with various writing times. These gratings were subsequently coated in approximately 70 nm of silver.

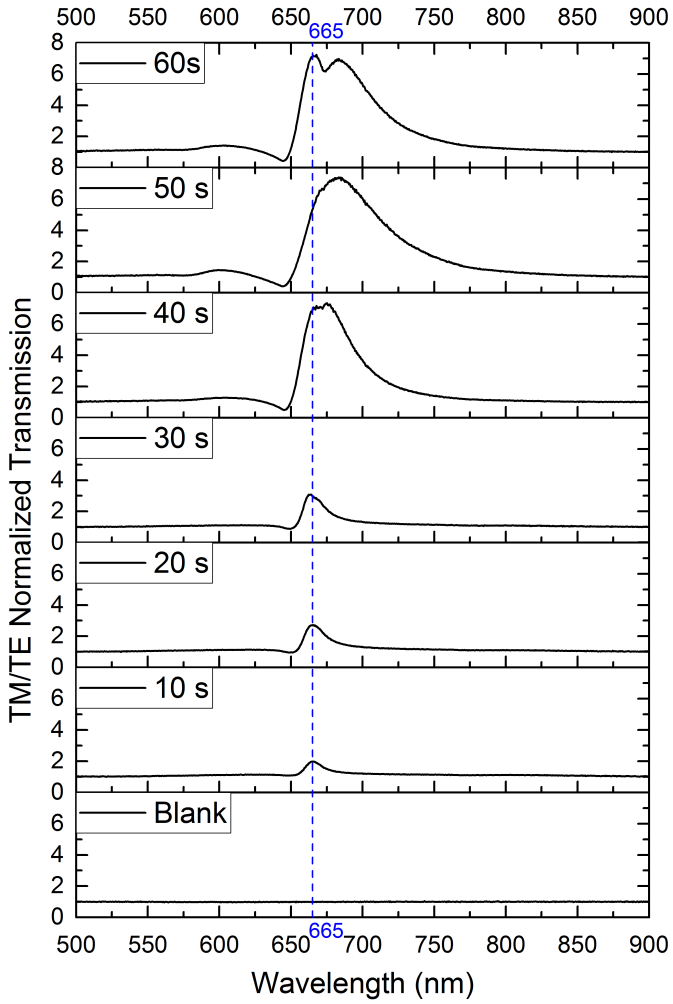

Figure 4.4: Transmission spectra from 650 nm pitched gratings with different exposure times (10s - 60s). Each grating has a 70 nm thick layer of silver deposited on the surface. A surface plasmon transmission peak occurs at 665 nm.

As seen in Fig. 4.4, between a 30-seconds and 40-seconds exposure time, the surface plasmon enhanced transmission peak doubles in height. However, the peak also appears to shift towards longer wavelengths, before splitting into two distinct peaks after 60 seconds of exposure.

The splitting of a surface plasmon transmission peak is expected once a grating is deep enough to generate a photonic energy gap [3]. However, the energy gap is suppose to be centered around the theoretical surface plasmon wavelength. The

shift in wavelength observed could be due to the Lloyd mirror set-up being rotated when the sample is placed in the holder. In addition, the dramatic increase in surface plasmon signal from 30 s to 40 s is not understood.

Reflection spectra were also taken from these same gratings and are depicted in Fig. 4.5 below.

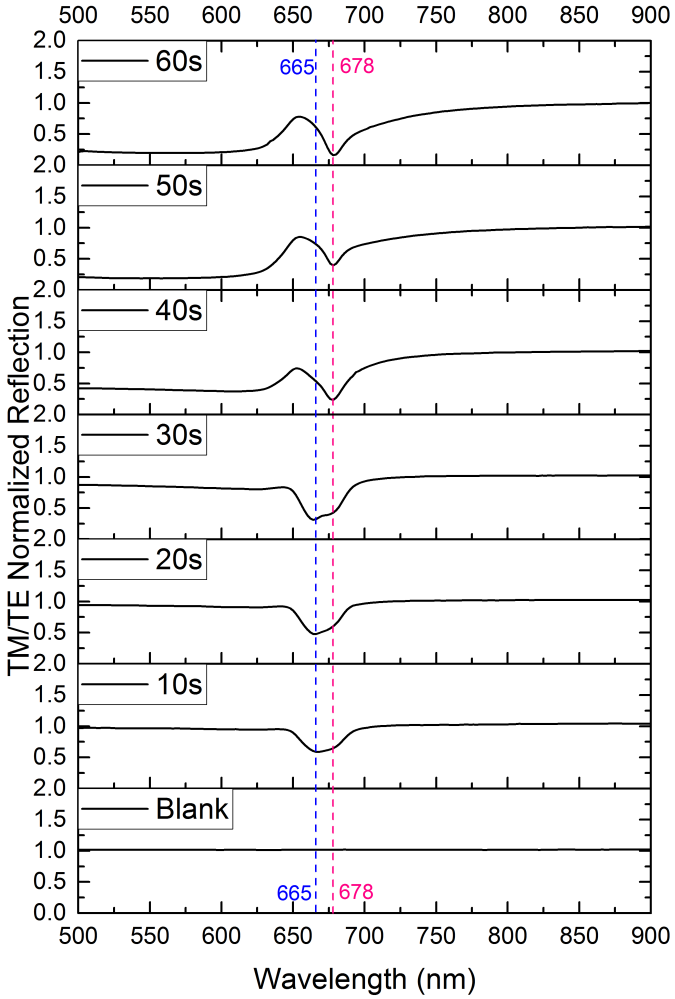

Figure 4.5: Reflection spectra from 650 nm pitched gratings with different exposure times (10s - 60s). Each grating has a 70 nm thick layer of silver deposited on the surface. A dip in reflection occurs at different wavelengths depending on the exposure time.

Again, there is a dramatic difference between the 30 second and 40 second

exposure that isn't understood. For this reason, all exposure times were chosen to be 30 seconds or shorter, to avoid observing other misunderstood phenomena.

4.1.3 Silver Thickness

To find the optimal silver layer thickness to deposit on top of the azobenzene gratings, constant-pitch 650 nm gratings were made by exposing an azobenzene sample to 10, 20 and 30 seconds. These were then coated with either a 40, 50, 60, or 70 nm thick layer of silver. Figure 4.6 below compares the the TM/TE normalized transmission spectra for the different gratings. In all three plots, the transmission peak from a grating coated in 60 nm of silver is the highest.

It should be noted that the wavelengths of these transmission peaks are not the same, with thinner layers of silver producing slightly higher surface plasmon wavelengths. This could again be due to the Lloyd mirror set-up rotating over time as these gratings were made. It could also be from differences in the azobenzene samples as all the gratings coated in 40 nm of silver were from the same sample, all those coated in 50 nm were from the same sample, etc. Finally, a thicker layer of silver may subtly change the shape of the grating surface, altering the wavelengths of the SPP waves. However, the transmission peaks from the gratings coated in 60 nm and 70 nm are centered about a wavelength of 670 nm, which is close to the theoretical 671.5 nm wavelength.

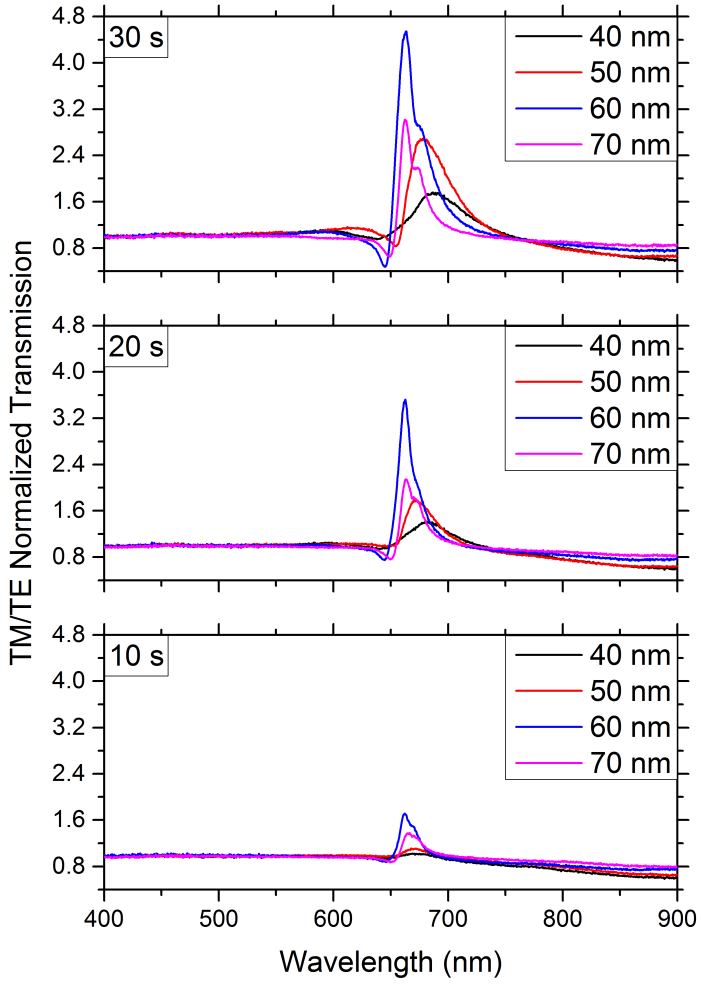

Figure 4.6: Transmission spectra from 650 nm pitched gratings made with different exposure times and different silver layer thicknesses.

Normally when shining light through a thin metallic film, one would expect that the thicker the metal, the lower the transmission would be. However, when surface plasmon polaritons are excited, the electric field enhancement due to surface plasmon excitation increases with metal film thickness, but so does the absorption of an electromagnetic wave transmitting through the metallic film [56, 59]. These competing factors give rise to an optimal thickness for transmitting surface plasmon polariton wavelengths. A previous literature value for the optimal silver thickness was found to be 50 nm for SPP waves excited at an air-

silver interface by a 380 nm grating on top of a glass substrate [56]. A possible reason why 60 nm was optimal here, instead of 50 nm, could be related to the azobenzene between the silver and and glass substrate, which was not present for the literature value. Another factor could simply be the differences in grating pitch chosen and therefore the surface plasmon wavelength, as the skin depth of an EM-wave in a conductor is shorter for smaller wavelengths [47].

4.1.4 Grating Pitch

Once all the parameters described above were optimized to produce the highest surface plasmon resonance transmission peak, a variety of gratings were made at different pitches. The plot below, Fig. 4.7, shows the transmission spectra obtained from gratings with pitches ranging from 550 nm to 800 nm. All of these gratings were made by exposing an azobenzene thin film to an interference pattern, produced by a 532 nm green Verdi laser, set to 0.75 Watts, or 312 mW/cm^2 irradiance, for 30 seconds. Afterwards, these gratings were coated with a 60 nm layer of silver.

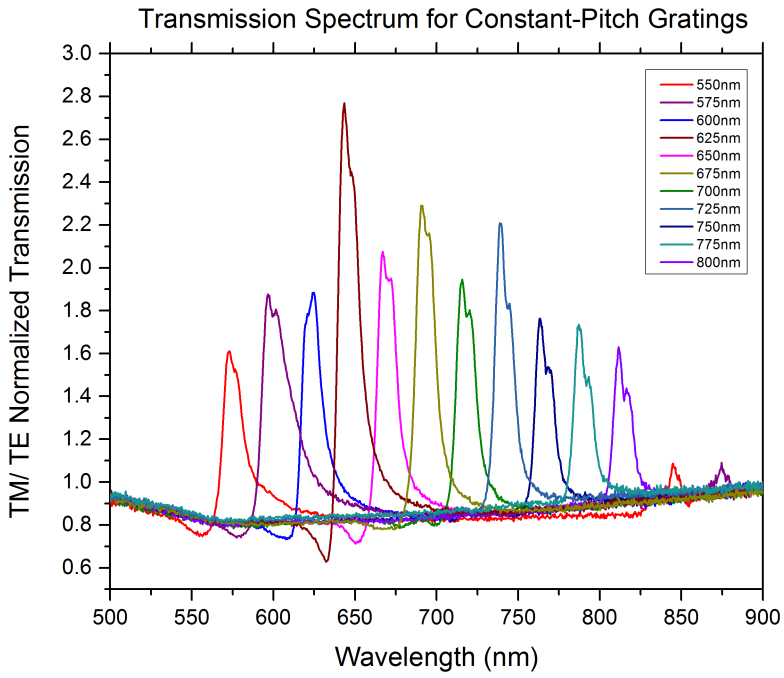

Figure 4.7: Transmission spectra obtained from gratings of various pitches.

In Fig. 4.7, we observe that each peak is actually composed of two closely

spaced peaks. Again, this is due to a photonic energy-gap that forms when the metallic grating is deep enough that it is no longer effectively flat with respect to the surface plasmon wavelength [60]. However, as seen in Fig. 4.8 the energy gap is indeed centered around the SPP wavelength predicted by Eq. 4.0.1.

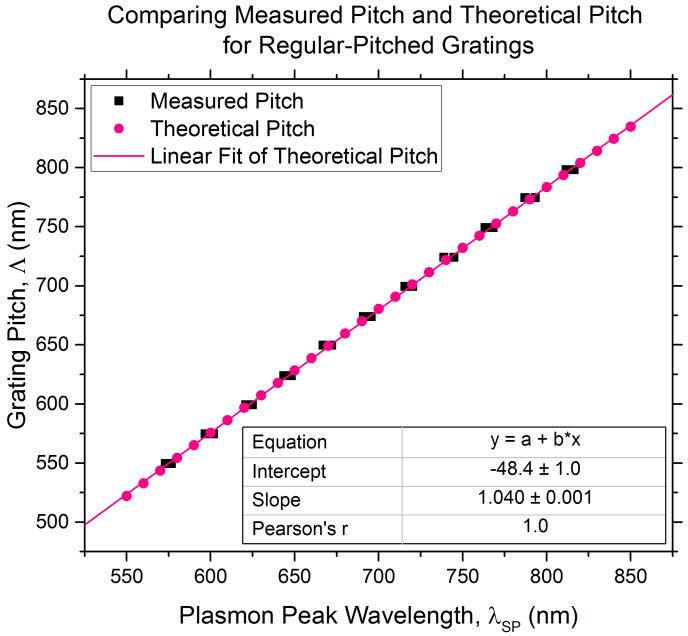

Figure 4.8: The theoretical and experimental relationship between the grating pitch and surface plasmon wavelength.

The second thing to notice from Fig. 4.7 is that the 550 nm and 575 nm gratings show an additional and smaller peak at 845 nm and 875 nm, respectively. These additional peaks are most likely from surface plasmon excitation at the azobenzene-silver interface rather than the air-silver interface. The wavelength of these peaks changes with changing grating pitch, much like the SPP peaks at the silver-air interface do, and since a lot of the incident light would be reflected by the above layer of silver, you would expect any plasmon peak at this interface to be small.

4.1.5 Angular Transmission Spectra

From Eq. 2.4.4, when the angle of incidence θ is non-zero, there should be two transmission peaks occurring at wavelengths that are symmetrical about the normal incidence wavelength peak. As the angle of incidence increases away from zero, the peaks will shift further away from the normal incidence wavelength. An

example is shown for a 750-nm pitched grating in Fig. 4.9. At a 10° angle of incidence, two transmission peaks occur at 648 nm and 898 nm. These are roughly symmetrical about the 771 nm peak at 0° angle of incidence.

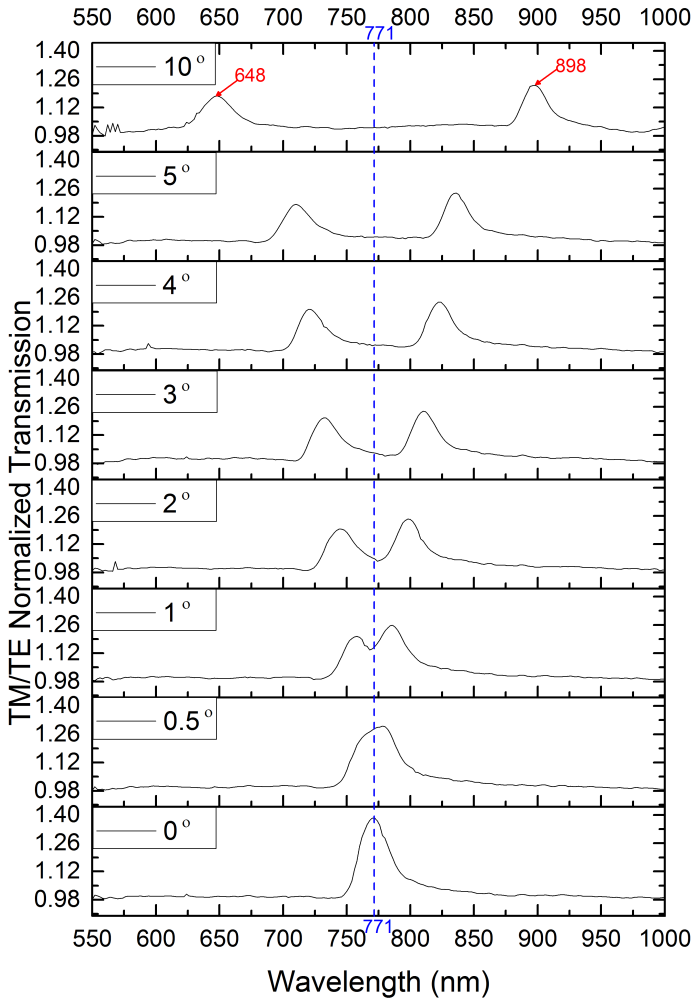

Figure 4.9: Transmission spectra from the same 750 nm grating at different angles of incidence.

4.2 Multi-Pitched Gratings

Before looking at chirped diffraction gratings, where the grating pitch gradually varies across the grating structure, the transmission spectra from superimposed parallel diffraction gratings, made with two distinct pitches, will be analysed. These gratings were made by first exposing an azobenzene sample area to a constant-pitch interference pattern, and then exposing the same azobenzene area to a different constant-pitch interference pattern.

Previous results have shown that parallel, superimposed diffraction gratings can be used to excite surface plasmon polariton waves at two different wavelengths. Furthermore, the diffraction intensities from the two grating structures can be made equal if the exposure time for the second, subsequently written grating, is limited to half the exposure time of the first grating [34].

Using this fact as a guideline, gratings with 650 nm pitches were made by exposing an azobenzene sample to a 650 nm pitched interference pattern for 30 seconds, using the Verdi laser set-up described in Section 3.2.1. Then, a subsequent exposure to a 680 nm pitched interference pattern was made with varying exposure times between 9 and 17 seconds. The TM/TE normalized transmission spectra for these gratings was taken using the fiber spectrometer set-up described in Section 3.4.4 and is plotted in Fig. 4.10 below.

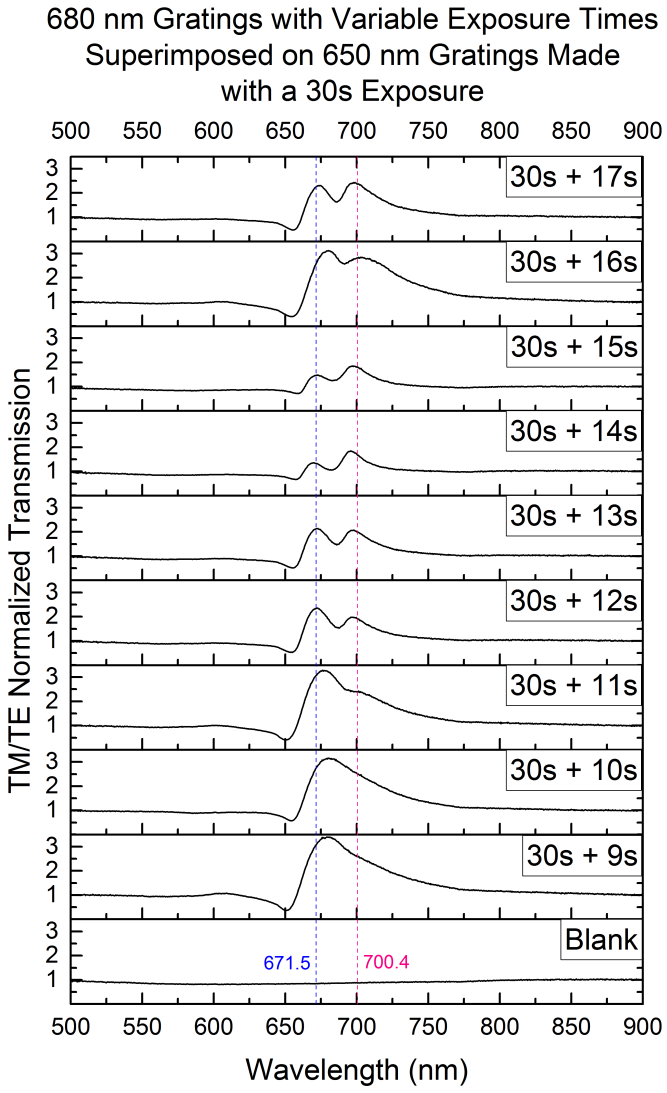

Figure 4.10: The transmission spectra for two superimposed and parallel grating structures, made with varyious exposure times for the second and larger grating pitch. The gratings were coated in 60 nm of silver to excite SPP waves.

Figure 4.10 shows that as the height of the two surface plasmon transmission signals becomes comparable, around 13 seconds for the second exposure, the height of each plasmon signal is significantly reduced. This is believed to be the result of some sort of signal averaging produced by the spectrometer itself, and will be explored further in later sections.

4.3 Chirped-Pitch Grating Calibration

4.3.1 Lens Distance

Before comparing a chirped-pitch grating to that of a constant-pitch grating, the distance of the lens from the sample was varied to see if there would be a noticeable effect on the grating pitch.

Figure 4.11 below depicts the TM/TE normalized transmission spectra obtained from an approximately 1 mm diameter area located at the approximate center of different chirped-pitch diffraction gratings, where each grating was made with the 4 mm diameter cylindrical lens at a different distance from the azobenzene sample. All other gratings variables like the exposure time, silver thickness, and the theoretical grating pitch, when the cylindrical lens is removed, remained the same for each grating. Looking at Fig. 4.11, the surface plasmon resonance transmission peak appears to broaden as the lens is brought closer to the sample. This indicates not only that grating pitch is chirped across a small 1 mm diameter region, but also that the rate of chirping is increasing across this small region as the lens is brought closer to the sample. Note here that the TM/TE normalized spectra taken on a blank area is a little lower than one. This is likely caused by the light source itself generating more TE light that TM light.

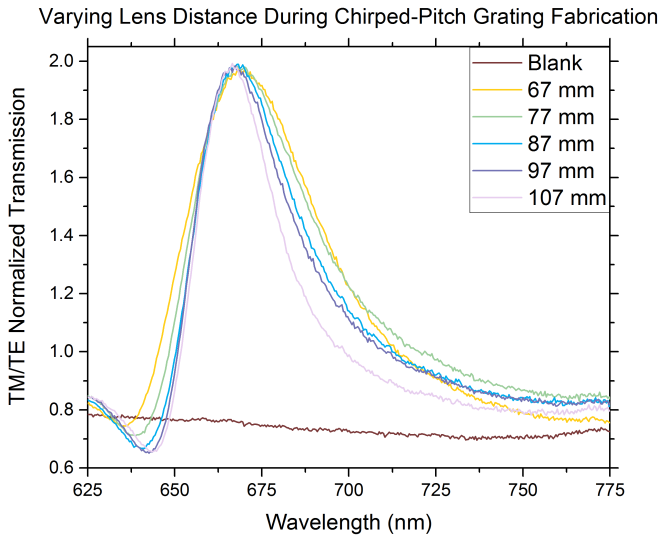

Figure 4.11: The transmission spectra taken from a 1 mm diameter, central area, on different chirped-pitch diffraction gratings, fabricated with the cylindrical lens at different distances during the azobenzene exposure. The theoretical pitch with cylindrical lens removed is 650 nm for all of the gratings.

As mentioned before in Section 2.6, this effect is expected. As the lens is moved closer to the azobenzene sample, the wave front from the lens will be more curved when it reaches the sample. This will increase the phase shift, Δ, responsible for the grating chirping.

4.3.2 Horizontal Placement of the Lens

The horizontal placement of the lens was not varied, but instead, placed so that the lens was close to the center of the direct half of the laser beam, with the rest of the direct half blocked by the custom aperture. If the horizontal lens was varied, a new custom aperture would have to be constructed and placed around the lens for every measurement. However, this ε value is used later to compare the range in pitch measured for chirped-pitch gratings with the range in pitch predicted by theory.

4.3.3 Exposure Time

With a cylindrical lens and its respective aperture placed in front of the direct half of the writing laser beam during the grating fabrication step, a significant portion of the light that would reach the azobenzene sample for a constant-pitch grating would not reach the sample for the chirped-pitch grating. The light striking the lens would undergo some reflection at the surface of the lens, and the light that would pass through, would diverged radially in the plane perpendicular to the lens' central, rotational axis of symmetry. The result of this is a lower irradiance on the surface of the azonbenzene sample during the grating fabrication step for chirped-pitch gratings. Therefore, to achieve an optimized surface plasmon resonance signal from these gratings, the exposure time needed to be optimized once again.

Figure 4.13 depicts the TM/TE normalized transmission spectra for chirped-pitch diffraction gratings made with different exposure times. For each grating, transmission spectra were taken at five different 1 mm diameter areas along the center of the grating structure. These five areas are depicted in Fig. 4.12 below, where the positions of these areas were never measured exactly, but instead, roughly estimated on each grating.

Also note that Fig. 4.12 depicts a grating length of 9.5 mm instead of the expected 10.3 mm length given in Section 2.6. This was because, when the first chirped-pitch gratings were fabricated, it was noticed that if the lens aperture was not covering all of the direct half of the laser beam, there would be a small section of the grating that would have a constant pitch. This constant-pitch area would generate a much higher surface plasmon resonance signal than the rest of the grating because of the increased irradiance involved in making that part of the grating. To completely avoid this, the lens aperture was made to block a

little, but visible portion, of the indirect beam. This made certain that all of the direct half of the beam was blocked, but shortened the length of the chirped-pitch gratings to a measured length of ($L = 9.5 \pm 0.4$) mm.

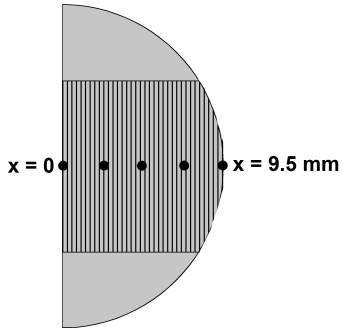

Figure 4.12: A representation of a typical, chirped diffraction grating with black dots marking, roughly, where five transmission spectra measurements were taken.

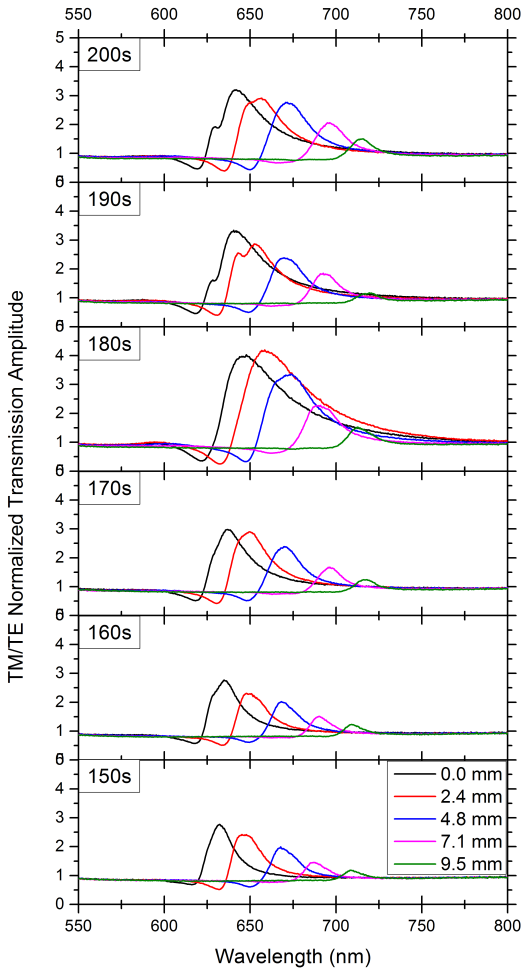

Figure 4.13: TM/TE normalized transmission measurements taken at five different locations along six, 650 nm pitched, chirped-pitch diffraction gratings, made with various exposure times.

Since the transmission spectra from the chirped-pitch gratings were to be compared with that of the constant-pitch gratings, with specific attention to the width of the transmission peaks, it was ideal to avoid the double transmission peaks attributed to a photonic energy gap. This was so a clear comparison could be made between the two grating spectra without an additional factor increasing the width of the transmission peaks for chirped-pitch gratings. Though the height of the transmission peaks are the highest from the grating made with a 180 s

exposure time, they are this way because a photonic energy gap is forming. With all of this in mind, exposure times of 160 s and under were chosen to make chirped-pitch gratings.

In Fig. 4.13, it should be noted that the surface plasmon resonance transmission peaks vary in height across all of the gratings, with the $x = 0$ mm grating position producing the highest resonance peak for all but one of the gratings (180 s exposure). Since this is the position closest to the mirror and to the center of the writing laser beam during grating fabrication, this effect is likely the result of an uneven intensity profile illuminating the azobenzene sample due to the Gaussian shape of the laser beam. This change in transmission across the length of the grating indicates that the grating is probably becoming more shallow from 0 mm to 9.5 mm.

Also from Fig. 4.13, it is apparent that gratings made with an exposure time greater than 180 seconds produce a photonic energy gap for areas closer to the x = 0 mm position, while other areas of the grating do not. This also indicates deeper grating grooves in these areas relative to others. This potential change in grating depth will be explored further in a later section.

Finally, it should noted from Fig. 4.13 that the surface plasmon resonance peak wavelength does shift as the light beam is moved across the grating. This indicates that indeed the grating spacing changes across the grating.

4.3.4 Final Chirped-Pitch Gratings

Chirped-pitch diffraction gratings were fabricated at five different pitches, 550 nm, 600 nm, 650 nm, 700 nm, and 750 nm. To clarify, these are the pitches that the gratings would have if the cylindrical lens was removed during the azobenzene exposure. These pitches are also expected to be the central pitch of the chirped-pitch gratings, assuming the lens was placed in the center of the direct half of the exposing laser beam. These gratings were all made with the cylindrical lens placed at a distance of $f = (69 \pm 1)$ mm from where the sample and mirror meet, and had an exposure time of 160 seconds. Each grating was then coated in 60 nm of silver so that surface plasmon resonant waves could be excited on the silver-air interface.

The range of pitches for these gratings was then measured using the HeNe Laser set-up described in Section 3.3. Figure 4.14, shown below, plots the measured pitch range versus the pitch the gratings would have if the cylindrical lens was removed. In addition, the theoretical pitch range, discussed in the Theory chapter of this thesis, is plotted for comparison. For the theoretical plot, Eq. 2.6.11 was used to obtain the phase shift, δ, with the distance of the cylindrical lens to the sample set at $f = 69$ mm, and the horizontal displacement of the lens set to $\varepsilon = 0.7$ mm. This ε value was found to give the best match to the measured data. Also, for comparison, the theoretical pitch range is plotted for $f = 69$ mm

and $\varepsilon = 0.0$ mm. During the actual grating fabrication process, the lens position could not be accurately measured, but instead placed roughly in the center of the direct half of the laser beam. The lens was not moved between the exposures for the different gratings, but was moved after, making it difficult to go back and measure the exact position of the lens for these specific gratings.

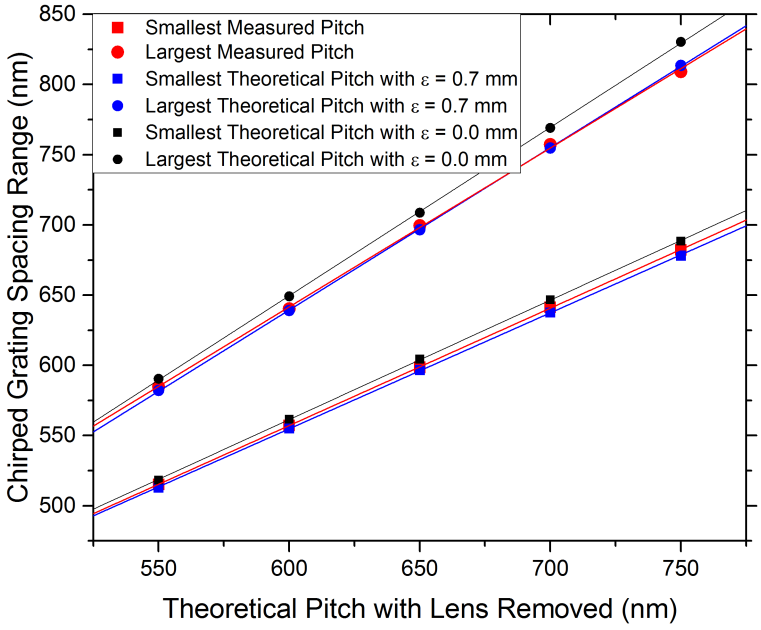

Figure 4.14: Comparing the measured range in grating pitch across chirped-pith diffraction gratings with what was theoretically predicted by the geometry of the grating fabrication set-up.

As discussed earlier in this chapter (Section 4.3.3), the theoretical pitch range assumes that the gratings are roughly 10.3 mm in length, but the actual fabricated gratings are only 9.5 mm in length. Therefore, the theoretical pitch range is not directly comparable to what was measured. However, from Fig. 4.14, the qualitative trend is found to be the same; the pitch range increases as the pitch, with the cylindrical lens removed, increases.

Using the measured pitch range for each grating, and assuming each grating is (9.5 ± 0.4) mm in length, the rate of chirping for each of these gratings was calculated. This is shown in Table 4.1, along with the measured range in pitch for these gratings. To see if there is a implicit trend, the rate of chirping was plotted against the theoretical pitch the gratings would have if the cylindrical lens was

removed, and is shown in Fig. 4.15.

Table 4.1: Measured change in grating pitch across chirped-pitch gratings

Grating Pitch if Lens Removed (nm)	Pitch Range (nm)	Rate of Chirping (nm/mm)
550	(515 ± 0.3) to (584.7 ± 0.6)	7.3 ± 0.4
600	(557 ± 0.2) to (640.4 ± 0.8)	8.7 ± 0.5
650	(598.7 ± 0.2) to (699.6 ± 0.5)	10.6 ± 0.5
700	(641.3 ± 0.1) to (757.3 ± 1.0)	12.2 ± 0.6
750	(682.3 ± 0.5) to (809.1 ± 1.3)	13.3 ± 0.8

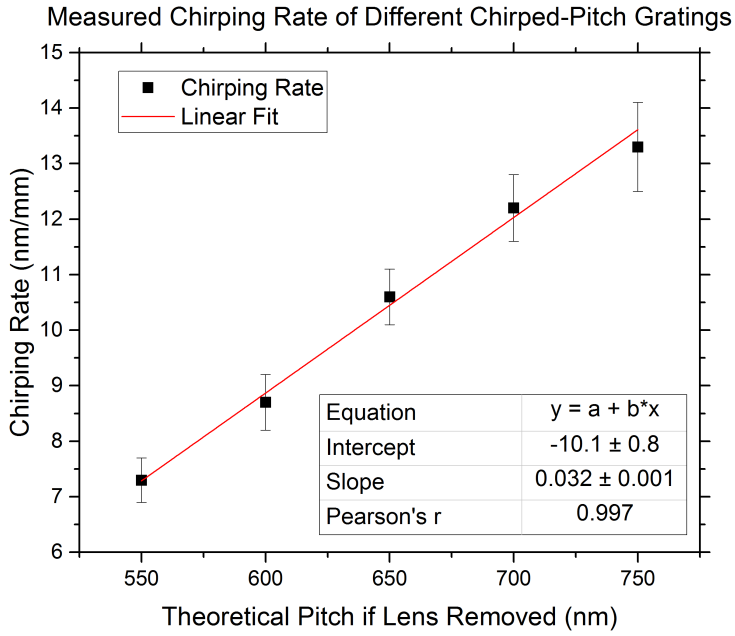

Figure 4.15: The calculated rate of chirping across different chirped-pitch diffraction gratings.

Looking at Fig. 4.15, in the range of grating pitches used in this thesis, the rate of chirping across a chirped-pitch grating appears to be linearly proportional to the theoretical pitch that the gratings would have if the cylindrical lens was removed.

Using the measured pitch range of a grating, and Eq. 4.0.1 at the beginning of this chapter for the relationship between grating pitch and surface plasmon

resonance wavelength, a theoretical surface plasmon polariton response range can be calculated. This theoretical range is shown in Figs. 4.16 (a)-(e) as a yellow band. Also shown are the TM/TE normalized transmission spectra for the five evenly spaced, approximately 1 mm diameter areas, depicted in Fig. 4.12 for each grating.

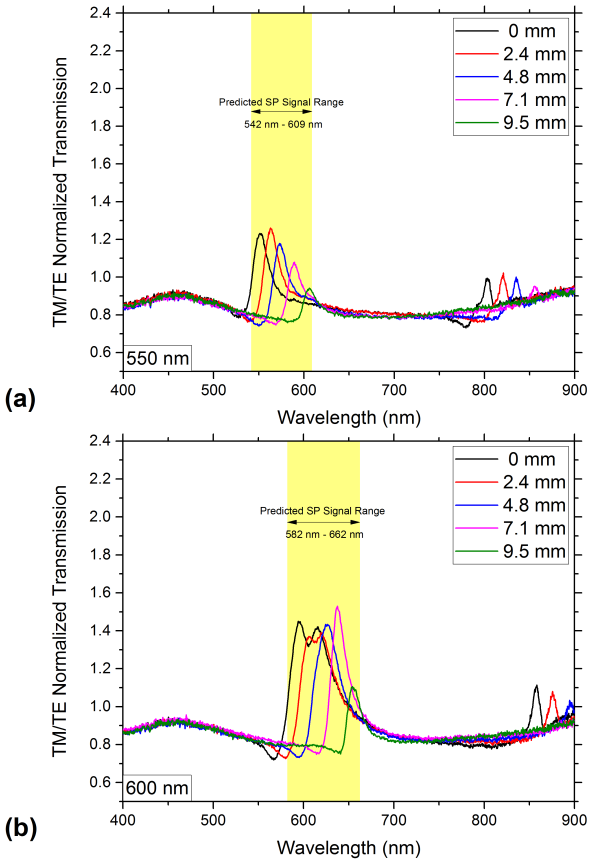

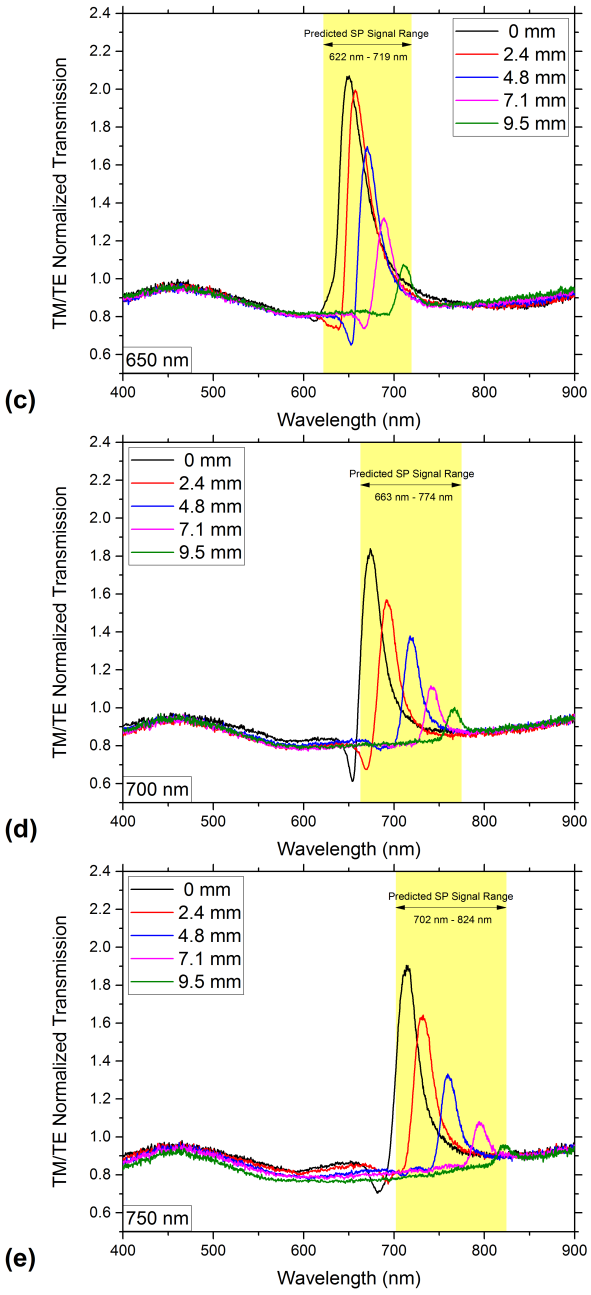

Figure 4.16: Transmission spectra at different areas along chirped-pitch diffraction gratings. The yellow sections indicate the theoretically predicted SPP transmission peak range for each grating.

From these plots, the surface plasmon peaks appear to span most of the theoretical predicted SPP wavelength range. However, the tip of the x = 0 mm peak and the x = 9.5 mm peak should be lying on the edge of the yellow region. Since this is not the case, it is likely that the 1 mm diameter beam of white light used for taking the transmission spectra were not on the very edges of the grating during these measurements. It was hard to see the exact edges of the gratings during these measurements because the gratings were not very deep and were coated with a reflective layer of silver. In addition, if an area of the probing light was partially off the grating, the transmission peak height would drop significantly. In hind-sight, a continuously-running spectrum could have been taken as the probing light was moved across the gratings to find the edges of the gratings.

Looking at Figs. 4.16 (a)-(e), the height of the transmission peaks across the gratings is not the same. Ideally, for an even bandwidth of surface plasmon response, the height of the peaks would be equal. To check whether a change in the grating depth was the cause of this, the average depth of these gratings at each of the five positions was measured using an AFM. The result of this is given below in Table 4.2, and shows that the depth of the gratings decreases from the x = 0 mm position to the x = 9.5 mm position on the gratings. This is likely the result of an uneven irradiation profile during the exposure of the azobenzene sample to the interfering laser light during the grating fabrication.

Table 4.2: Average grating depth over a 5-micron square area at various locations on a chirped-pitch grating

AFM Scan Position x (mm)	0	2.4	4.8	7.1	9.5
Average Grating Depth (nm)	59.9	47.8	33.4	28.0	19.7

4.4 Comparing Chirped and Constant-Pitched Gratings

To compare the surface plasmon response of a chirped-pitch diffraction grating with that of a constant-pitch diffraction grating, the set-up described in Section 3.4.3 of the Procedure chapter was used to take the TM/TE normalized transmission spectra from an entire grating. However, it was made clear that the height of the transmission peaks from the constant-pitched gratings, even those made with an exposure time of only 10 s, would be much larger than those from chirped-pitch gratings. This was because the constant-pitch gratings were entirely one single grating spacing, capable of exciting surface plasmon resonance waves at a single wavelength across the entire grating. The chirped-pitched gratings however, only have a small area capable of exciting surface plasmons at a particular wavelength. To try and overcome this difference in peak height, the variable neutral density

filter in the set-up was changed in order to lower the irradiance of the light illuminating the constant-pitched gratings. This however, was found to alter the intensity profile of the light as a function of wavelength. To avoid this, the variable filter was then set to remain constant, and instead, the rectangular beam of white light was moved partially off of the constant-pitch gratings until the transmissions peaks were comparable in height to those from chirped-pitched gratings. Looking at Fig. 4.17 as a reference, moving the probing light partially off a grating did not change the wavelength of the transmission peak, nor did it change the full-width-at half-max (FWHM) of the transmission peak. However, by reducing the height of the transmission peak, a better visual comparison between chirped and constant-pitched gratings could be made in real time as the measurements were taken.

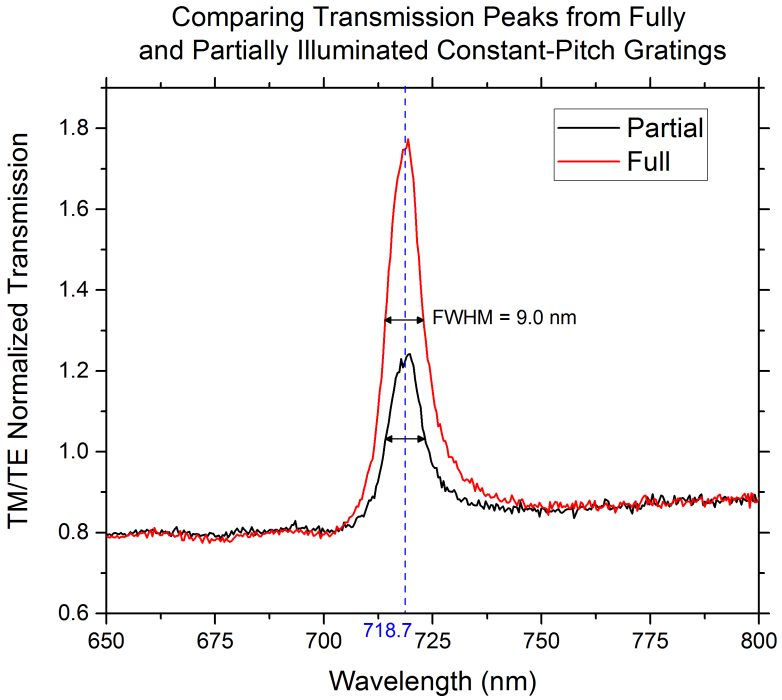

Figure 4.17: The TM/TE normalized transmission spectra from a partially and fully illuminated 700 nm constant-pitch diffraction grating, made with a 30 sec. exposure and coated in 60 nm of silver.

Figure 4.18 below shows the TM/TE normalized transmission spectra taken from fully illuminated chirped-pitch diffraction gratings with expected central pitches of 550 nm, 600 nm, 650 nm, 700 nm, and 750 nm. Overlain on these plots are TM/TE normalized transmission spectra for constant-pitch gratings

with comparable grating pitches to those of the chirped-pitch gratings. Finally, the theoretical surface plasmon excitation range that is expected for each chirped-pitch grating is depicted as a yellow band across each plot.

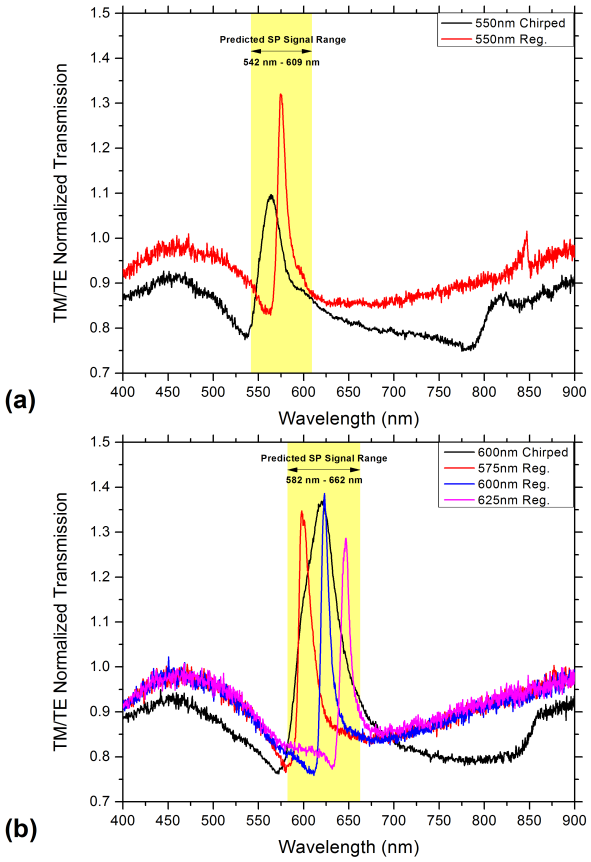

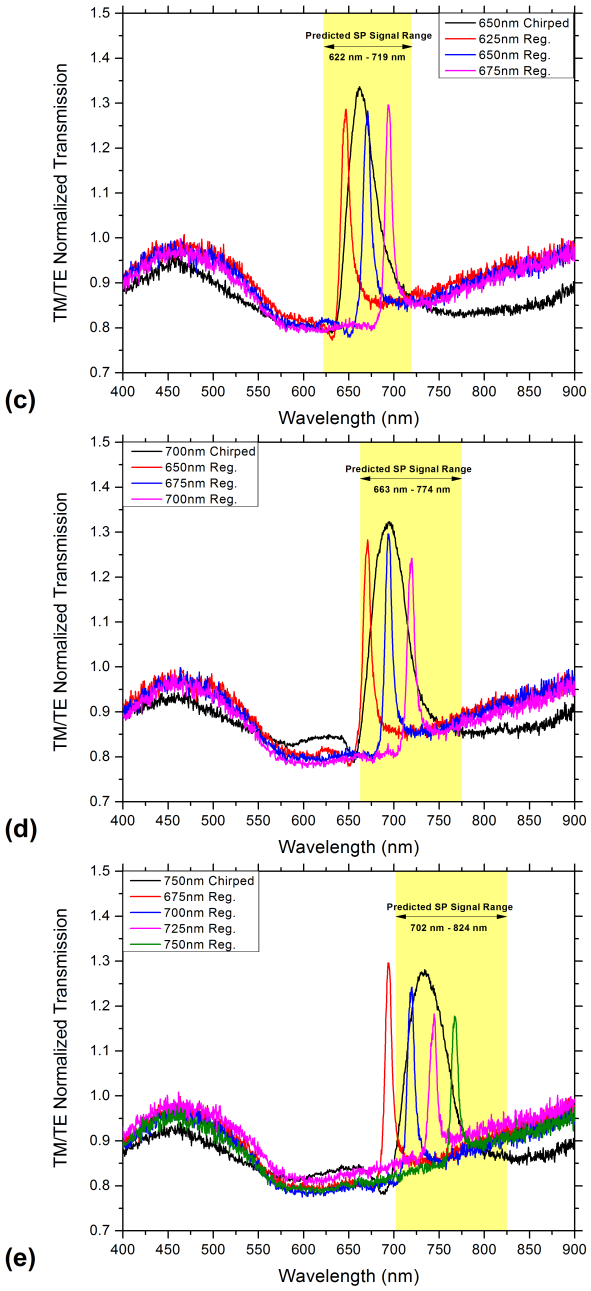

Figure 4.18: Various TM/TE normalized transmission spectra for fully illuminated, chirped-pitch diffraction gratings (black) with their theoretical surface plasmon response range (yellow), as well as various transmission spectra for constant-pitch gratings.

Looking at the plots in Figs. 4.18 (a)-(e), the chirped-pitch gratings do appear to simultaneously excite surface plasmon polaritons over a wider range of wavelengths than the constant-pitch gratings. Table 4.3 below gives the average FWHM of the chirped and constant-pitch gratings. Indeed, the chirped-pitch gratings generate a wider transmission peak, indicating a wider wavelength band of surface plasmon polariton excitation. Note, that for whatever reason, the transmission from the 550 nm chirped-pitch grating is less wide that the other chirped-pitch gratings. Also note, that the double transmission peak caused by a photonic energy gap, shown in Fig. 4.16-(b), for the 600 nm chirped-pitch grating results in a shoulder on the fully illuminated transmission spectra.

Table 4.3: The FWHM of transmission peaks for chirped and constant-pitched gratings

Pitch with cylindrical lens removed (nm)	550	575	600	625	650	675	700	725	750
Average FWHM for constant-pitch gratings (nm)	11 ± 2	16 ± 3	10.4 ± 0.9	11 ± 2	9.5 ± 1.4	8.4 ± 1.0	9.2 ± 1.4	8.5 ± 1.2	8.5 ± 0.7
Average FWHM for chirped-pitched gratings (nm)	27 ± 4	-	46 ± 4	-	34 ± 3	-	43 ± 4	-	51 ± 5

Looking at Figs. 4.18 (a)-(e), however, the transmission peaks clearly do not span the entire theoretical surface plasmon wavelength range. This could be due to the light source potentially not illuminating the entire diffraction grating while the transmission spectra were taken. Also, looking at Figs. 4.16 (a)-(e), a lower transmission is expected at higher wavelengths within the theoretical range, since the response from these individual areas was lower, due to the previously discussed shallower grating depths. Finally, the chirped-pitch gratings were not rectangular like the aperture that illuminated them, but instead curved at the side with the lower transmission response. This would mean that for higher grating pitches located on the curved side of the grating, less of that grating pitch existed to be illuminated, and therefore less surface plasmon response from these pitches would be expected.

Comparing Fig. 4.16 to Fig. 4.18, it can be noted that the height of the transmission peaks coming from the fully illuminated gratings are lower than the transmission peaks coming from individual areas on the same gratings. As mentioned in Section 4.2, the spectrometer may have been averaging the light signal in some way, which may account for the lower height of the transmission

peaks from fully-illuminated gratings.

To explore this further, the TM/TE normalized transmission spectra, shown in Figs. 4.16 (a)-(e), obtained from five individual areas on a chirped-pitch grating were averaged. These plots are compared with the full transmission spectra and are shown below in Figs. 4.19 (a)-(e).

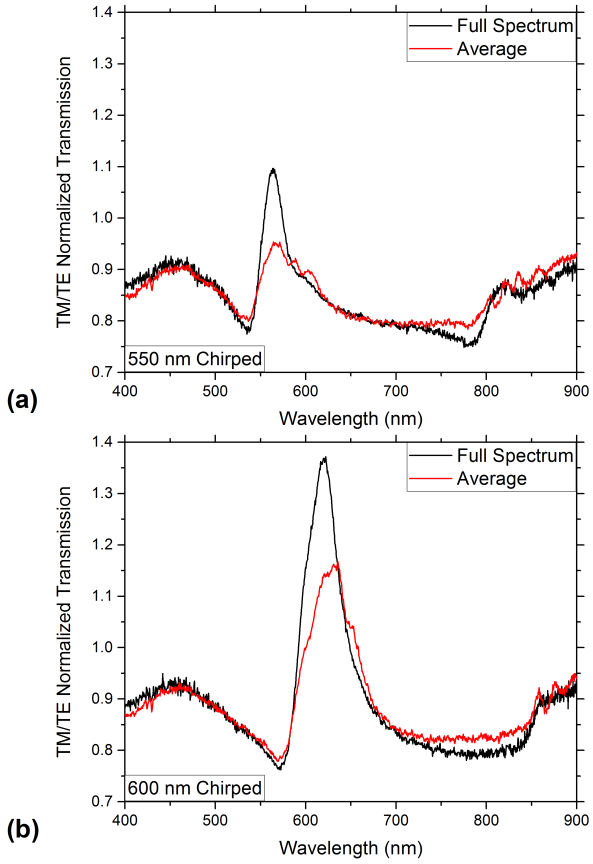

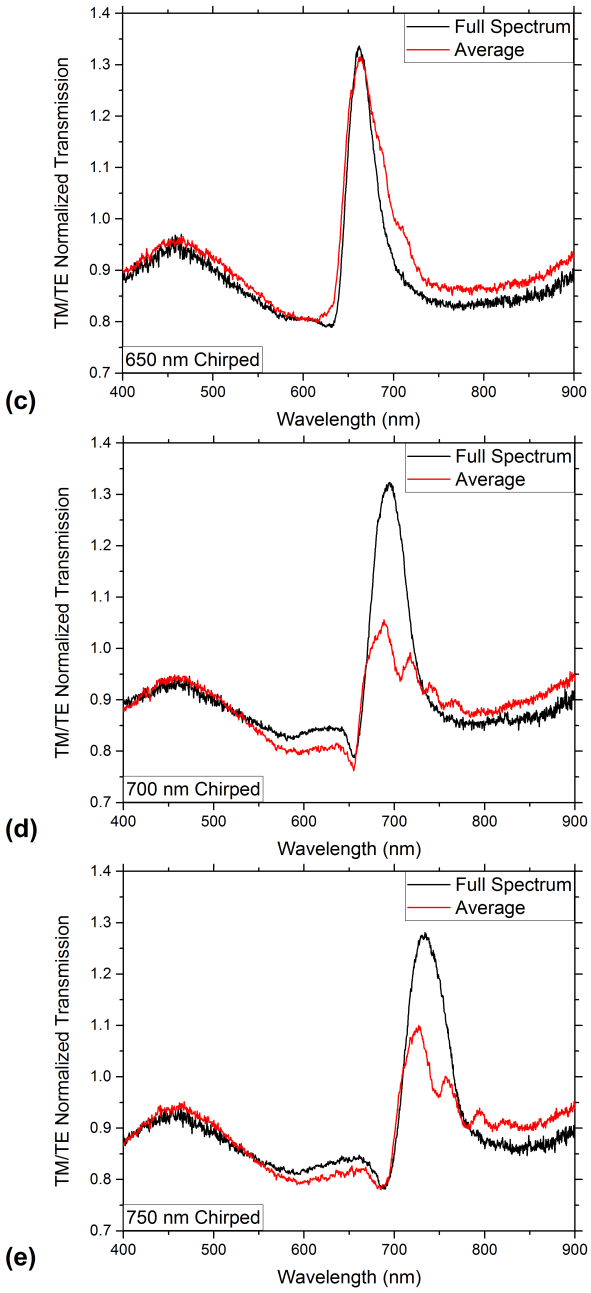

Figure 4.19: Comparing the fully illuminated transmission spectra from chirped-pitch gratings to the average of the transmission spectra taken at five individual, 1 mm diameter areas on the same gratings.

Looking at Figs 4.19 (a)-(e), averaging over five signals is obviously not enough to generate the observed spectra. The averaged peaks are in general, lower in height and wider in wavelength than the observed full transmission spectra. One could assume that this lack in height is a result of only averaging over 5 spectra. However, in another attempt to understand what was going on, information from the five transmission peaks observed in Fig. 4.16-(e), specifically the wavelength, width, and height of these peaks was used to generate expected transmission peaks at other areas along the grating. Figures 4.20 (a)-(d) show how this was done. Specifically, Fig. 4.20-(a) shows the set of spectra that was used. This is the same set of five spectra from the 750 nm chirped-pitch grating, shown in Fig. 4.16-(e), but with a blank spectrum, taken from a silver coated azobenzene area with no grating, subtracted from each. Figures 4.20 (b)-(d) show the trend of the wavelength, width and peak height, respectively.

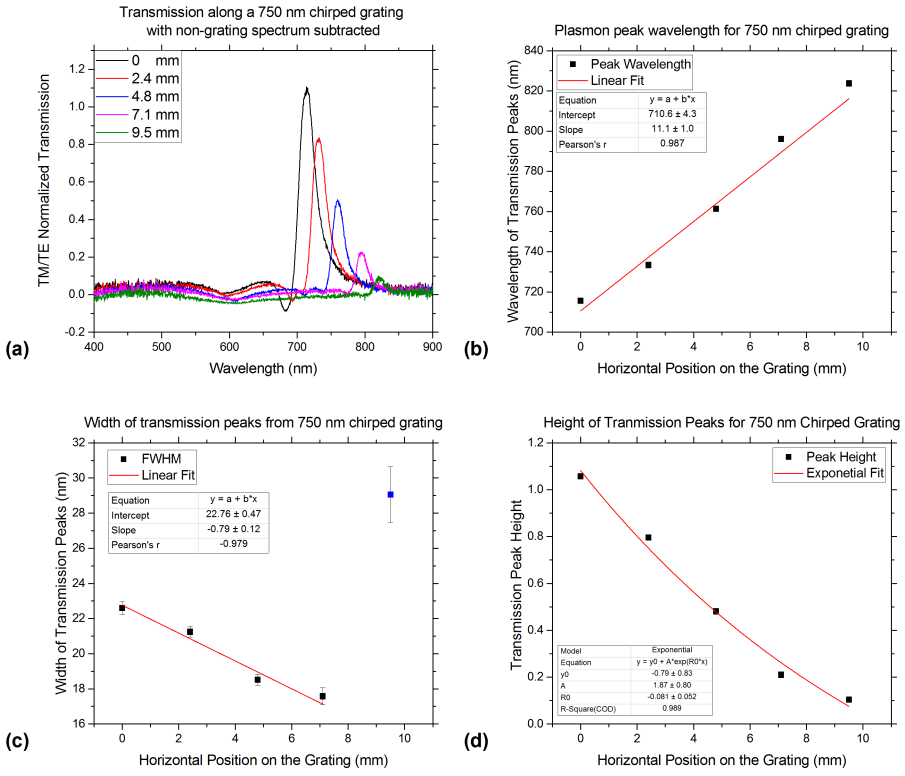

Figure 4.20: (a) The TM/TE normalized transmission spectra from five individual, 1 mm diameter, areas on a 750 nm chirped-pitch grating, with a TM/TE normalized blank spectrum subtracted from each plot; (b)The trend in the transmission peak wavelength; (c) The trend in transmission peak width. The linear fit, shown in red, ignores the on data point, coloured blue, that is an outlier from the rest of the data; (d) The trend in the transmission peak height.

Making the simplifying assumption that each transmission peak is a perfect Lorentzian function, peaks at each area along the grating could be generated. From x = 0 mm to x = 9.5 mm, by an interval of 0.1 mm, 96 peaks were generated, added together, and then divided by 96. The result is shown if Fig. 4.21 below along with the full, TM/TE normalized transmission spectrum obtained from the 750 nm grating (with the TM/TE normalized blank spectrum subtracted).

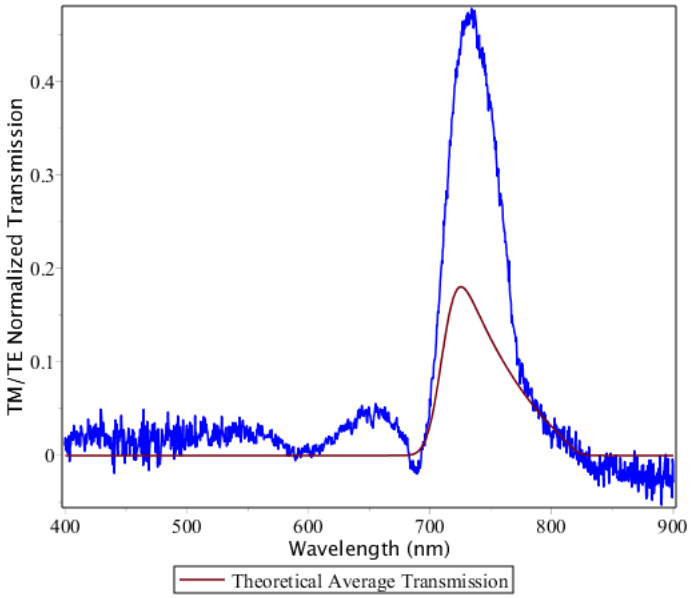

Figure 4.21: Comparing the average of the numerically generated transmission peaks (red) with the actual TM/TE normalized transmission spectra obtained over an entire 750 nm chirped-pitch diffraction grating (blue), where the TM/TE tranmsission spectra from an area with no grating has been subtracted.

From Fig. 4.21, it can be seen that, averaging across more peaks decreases the height of the transmission even further. Furthermore, the shape of the signal is considerably different. Therefore, a simple averaging of the signal is not what is happening. Instead, it is likely that the sensitivity of the CCD spectrometer depended on the location and direction of the incoming light, and some sort of weighted average was occurring instead. With this in mind,the plasmon response shown for the fully illuminated chirped-pitch diffraction gratings may actually be greater than what was measured.

5 Conclusion

5.1 Summary

The goal of this thesis was to demonstrate the simultaneous excitation of surface plasmon waves over a bandwidth of wavelengths from a single, chirped-pitch diffraction grating structure, and to compare this with the bandwidth generated from constant-pitch gratings. In addition, a novel technique for fabricating chirped-pitch diffraction gratings was utilized which proved to be more time efficient than other methods, requiring only a single fabrication step. Specifically, the gratings were made by exposing a thin film of an azobenzene containing molecular glass to a chirped-pitch interference pattern. Due to the cis-trans isomerization that occurs in the azobenzene molecule upon exposure to an absorbing wavelength of light, the interference pattern was photo-mechanically imprinted onto the surface of the thin film as a chirped-pitch, sinusoidal surface relief grating. To generate the chirped-pitch interference pattern, the same Lloyd mirror set-up used to generate a constant-pitch interference pattern was employed, but with a cylindrical lens placed in front of half of the incoming, coherent laser light beam. Once a grating was made, it was coated in a thin layer of silver to enable surface plasmon polariton excitation at the silver-air interface of the grating.

To compare the SPP excitation wavelength range of a chirped-pitch diffraction grating to that of a constant-pitch diffraction grating, the TM/TE-normalized transmission spectra from both constant and chirped-pitch gratings were obtained. This meant that the transmission spectra for both TM-polarized light and TE-polarized light were taken separately and then divided by each other. In this case, TM-polarized light corresponded to linearly polarized light with the electric field vector pointing parallel to the grating vector, and TE-polarized light was linearly polarized light with the electric field vector pointing perpendicular to the grating vector. Since SPP waves on a grating can only be excited by TM-polarized light, the SPP peaks only appear in the TM-polarized spectra and other, non-polarization dependent phenomenon will be divided out. By observing the theoretically predicted transmission peaks at the surface plasmon wavelengths, the bandwidths of these peaks could be compared directly.

However, before a comparison was made, steps were taken to optimize the surface plasmon peak generated from both types of gratings. This meant varying parameters like the inscribing laser's irradiance, the azobenzene exposure time, and the thickness of the subsequent layer of silver on top of the gratings in order to generate large and distinguishable transmission peaks. Through this optimization, an irradiance of 312 mW/cm^2 was chosen for the 532 nm laser. This irradiance was measured in an area before the cylindrical lens placement, and before the Lloyd mirror and sample in the grating fabrication set-up. With this irradiance, exposure times as short as 30 seconds were sufficient in generating constant-pitch gratings with grating pitches ranging from 525 nm to 750 nm. For chirped-pitch diffraction gratings, 160 seconds of exposure was used to generate gratings with an approximate central pitch of 550 nm, 600 nm, 650 nm, 700 nm, and 750 nm. The chirping rate for these gratings was found to vary linearly with the central pitch, with a maximum chirping rate of (13.3 $\pm$ 0.8) nm/mm calculated for the 750 nm chirped-pitch grating. For both types of gratings, a 60 nm thick layer of silver was found to give the largest plasmon peak height in transmission.

When a transmission spectra was obtained from an entire constant and chirped-pitch grating, it was found that the bandwidth, measured by the full-width-half-max of the transmission peaks, was wider for the chirped-pitch gratings than it was for the constant-pitch gratings (2.5 to 6 times wider depending on the grating). However, the width of the transmission peaks from the chirped-pitch gratings did not span the entire wavelength range that was predicted by the theory and the transmission spectral shape was not the uniform band that was expected. This is largely attributed to an uneven grating depth that was measured across the chirped-pitch gratings. From one side of a grating to the other, the grating depth decreased. This corresponded to a decrease in the transmission peak height when transmission spectra were taken from individual, 1 mm diameter areas across a grating. However, the observed transmission peak for a fully illuminated chirped-pitch grating was also noticeably lower in height than the transmission peaks taken from individual areas on the same grating. This was likely the result of the CCD fiber spectrometer that was used to obtain the transmission spectra.

5.2 Conclusions

Chirped-pitch diffraction gratings with chirping rates as high as (13.3 $\pm$ 0.8) nm/mm were fabricated. The pitch of these gratings was varied by changing the angle of the Lloyd mirror set-up, the diameter of the inscribing laser beam, and the position of the cylindrical lens. These gratings were able to simultaneously excite surface plasmon polaritons across a bandwidth of wavelengths. This bandwidth, when compared to their constant-pitch counterparts, increased by a factor ranging from 2.5 to 6 depending on the grating. However, there was a lack of control over

the grating depth across each grating, and therefore a lack of control over SPP coupling efficiency. As well, there is an apparent trade-off between coupling a bandwidth of surface plasmon polaritons and the coupling efficiency at individual wavelengths.

5.3 Future Work

Future work could focus on computational modelling of the expected plasmonic response of chirped-pitch diffraction gratings in an effort to better understand the effects that chirping the pitch has on SPP excitation, propagation, and re-emission.

Additional work is also needed to experimentally validate the use of chirped-pitch diffraction gratings in thin film solar cells. Previous work has shown that metallic gratings capable of simultaneously exciting multiple SPP waves can enhance the efficiency of thin film solar cells [34, 36], but chirped pitch gratings have yet to be tested in a photo-voltaic cell. Other application avenues could also be explored, as chirped-pitch gratings have a variety of other applications ranging from organic light emitting diodes [61], tunable resonance filters [41], infrared absorption spectroscopy [33] and sub-wavelength optics [43].

Finally, the fabrication method employed in this thesis offers a wide variety of experimentation when it comes to making diffraction gratings of different shapes and pitches. If an interference pattern can be generated, it can be photo-mechanically imprinted onto an azobenzene thin film surface. In the future, to help overcome both the wavelength dependence and the polarization dependence of surface plasmon polariton excitation via the grating method, a chirped-pitch circular grating could be fabricated [62], coated in silver and have its plasmonic response investigated.

References

[1] S. A. Maier. Plasmonics: Fundamentals and applications. 2007. ISBN: 0-387-37825-1.

[2] Pieter G. Kik and Mark L. Brongersma. *Surface Plasmon Nanophotonics*, chapter 1: Surface Plasmon Nanophtonics. Springer Netherlands, 2007. doi: 10.1007/978-1-4020-4333-8.

[3] Alain Dereux William L. Barnes and Thomas W. Ebbesen. Surface plasmon subwavelength optics. *Nature*, 424:824–830, Aug 2003.

[4] S. L. Cunningham, A. A. Maradudin, and R. F. Wallis. Effect of a charge layer on the surface-plasmon-polariton dispersion curve. *Phys. Rev. B*, 10: 3342–3355, Oct 1974. doi: 10.1103/PhysRevB.10.3342.

[5] R. W. Wood. On a remarkable case of uneven distribution of light in a diffraction grating spectrum. *Proceedings of the Physical Society of London*, 18:269–275, 1902.

[6] Lord Rayleigh O.M. P.R.S. Iii. note on the remarkable case of diffraction spectra described by prof. wood. *Philosophical Magazine Series 6*, 14(79): 60–65, 1907. doi: 10.1080/14786440709463661.

[7] A. Hessel and A. A. Oliner. A new theory of wood's anomalies on optical gratings. *Appl. Opt.*, 4(10):1275–1297, Oct 1965. doi: 10.1364/AO.4.001275.

[8] U. Fano. The theory of anomalous diffraction gratings and of quasi-stationary waves on metallic surfaces (sommerfeld's waves). *J. Opt. Soc. Am.*, 31(3): 213–222, Mar 1941. doi: 10.1364/JOSA.31.000213.

[9] A. Sommerfeld. Ueber die fortpflanzung elektrodynamischer wellen längs eines drahtes. *Annalen der Physik*, 303(2):233–290, 1899. ISSN 1521-3889. doi: 10.1002/andp.18993030202.

[10] J. Zenneck. Über die fortpflanzung ebener elektromagnetischer wellen längs einer ebenen leiterfläche und ihre beziehung zur drahtlosen telegraphie. *Annalen der Physik*, 328(10):846–866, 1907. ISSN 1521-3889. doi: 10.1002/andp.19073281003.

[11] E.G. Loewen and E. Popov. *Diffraction Gratings and Applications*. Optical Science and Engineering. Taylor & Francis, 1997. ISBN 9780824799236.

[12] R. H. Ritchie. Plasma losses by fast electrons in thin films. *Phys. Rev.*, 106: 874–881, Jun 1957. doi: 10.1103/PhysRev.106.874.

[13] C. J. Powell and J. B. Swan. Effect of oxidation on the characteristic loss spectra of aluminum and magnesium. *Phys. Rev.*, 118:640–643, May 1960. doi: 10.1103/PhysRev.118.640.

[14] R. H. Ritchie, E. T. Arakawa, J. J. Cowan, and R. N. Hamm. Surface-plasmon resonance effect in grating diffraction. *Phys. Rev. Lett.*, 21:1530–1533, Nov 1968. doi: 10.1103/PhysRevLett.21.1530.

[15] Jiri Homola O. S.Wolfbeis, editor. *Springer Series on Chemical Sensors and Biosensors: Surface Plasmon Resonance Based Sensors*, volume 4. Springer Berlin Heidelberg, 2006. doi: 10.1007/b100321. ISBN: 978-3-540-33919-9.

[16] M. Fleischmann, P.J. Hendra, and A.J. McQuillan. Raman spectra of pyridine adsorbed at a silver electrode. *Chemical Physics Letters*, 26(2):163 – 166, 1974. ISSN 0009-2614. doi: http://dx.doi.org/10.1016/0009-2614(74)85388-1.

[17] Pascal Anger, Palash Bharadwaj, and Lukas Novotny. Enhancement and quenching of single-molecule fluorescence. *Phys. Rev. Lett.*, 96, Mar 2006. doi: 10.1103/PhysRevLett.96.113002.

[18] J. L. Coutaz, M. Neviere, E. Pic, and R. Reinisch. Experimental study of surface-enhanced second-harmonic generation on silver gratings. *Phys. Rev. B*, 32:2227–2232, Aug 1985. doi: 10.1103/PhysRevB.32.2227.

[19] Nicholas Fang, Hyesog Lee, Cheng Sun, and Xiang Zhang. Sub–diffraction-limited optical imaging with a silver superlens. *Science*, 308(5721):534–537, 2005. ISSN 0036-8075. doi: 10.1126/science.1108759.

[20] Junji Tominaga. *Surface Plasmon Nanophotonics*, chapter 16: Localized Surface Plasmons for Optical Data Storage Beyond the Diffraction Limit. Springer Netherlands, 2007. doi: 10.1007/978-1-4020-4333-8.

[21] Cheng Sun Qi Luo Werayut Srituravanich, Nicholas Fang and Xiang Zhang. Plasmonic nanolithography. *Nano Letters*, 2004.

[22] H. Ditlbacher, J. R. Krenn, G. Schider, A. Leitner, and F. R. Aussenegg. Two-dimensional optics with surface plasmon polaritons. *Applied Physics Letters*, 81(10):1762–1764, 2002. doi: 10.1063/1.1506018.

[23] Andreas Hohenau, Joachim R. Krenn, Andrey L. Stepanov, Aurelien Drezet, Harald Ditlbacher, Bernhard Steinberger, Alfred Leitner, and Franz R. Aussenegg. Dielectric optical elements for surface plasmons. *Opt. Lett.*, 30 (8):893–895, Apr 2005. doi: 10.1364/OL.30.000893.

[24] Qing-Dong Ou, Yan-Qing Li, and Jian-Xin Tang. Light manipulation in organic photovoltaics. *Advanced Science*, 3(7), 2016. ISSN 2198-3844. doi: 10.1002/advs.201600123.

[25] E. Kretschmann and H. Raether. Radiative decay of non radiative surface plasmons excited by light. *Zeitschrift für Naturforschung*, 1968. 23a(12), pp. 2135-2136.

[26] Thomas Arno Klar. *Nanophotonics with Surface Plasmons: Advances in Nano-Optics and Nano-Photonics*, chapter 8: Biosensing with Plasmonic Nanoparticles. Elsevier B. V., 2007. doi: 10.1016/S1871-0018(06)02008-5.

[27] Andreas Otto. Excitation of nonradiative surface plasma waves in silver by the method of frustrated total reflection. *Zeitschrift für Physik A Hadrons and nuclei*, 216(4):398–410, 1968. doi: 10.1007/BF01391532.

[28] Jiandong Ye Mingbin Yu Guo-Qiang Lo Fang-Fang Ren, Kah-Wee Ang and Dim-Lee Kwong. Split bull's eye shaped aluminum antenna for plasmon-enhanced nanometer scale germanium photodetector. *Nano Lett.*, 11(3), Feb 2011. doi: 10.1021/nl104338z.

[29] Robert L. Nelson Weibin Chen, Don C. Abeysinghe and Qiwen Zhan. Plasmonic lens made of multiple concentric metallic rings under radially polarized illumination. *Nano Lett.*, 9(12):4320–4325, Oct 2009. doi: 10.1021/nl903145p.

[30] Jennifer M. Steele, Zhaowei Liu, Yuan Wang, and Xiang Zhang. Resonant and non-resonant generation and focusing of surface plasmons with circular gratings. *Opt. Express*, 14(12):5664–5670, Jun 2006. doi: 10.1364/OE.14.005664.

[31] Yongqi Fu, Yu Liu, Xiuli Zhou, Zongwei Xu, and Fengzhou Fang. Experimental investigation of superfocusing of plasmonic lens with chirped circular

nanoslits. *Opt. Express*, 18(4):3438–3443, Feb 2010. doi: 10.1364/OE.18.003438.

[32] Ido Dolev, Michael Volodarsky, Gil Porat, and Ady Arie. Multiple coupling of surface plasmons in quasiperiodic gratings. *Opt. Lett.*, 36(9):1584–1586, May 2011. doi: 10.1364/OL.36.001584.

[33] Joseph W. Petefish and Andrew C. Hillier. Multipitched diffraction gratings for surface plasmon resonance-enhanced infrared reflection absorption spectroscopy. *Analytical Chemistry*, 87(21):10862–10870, Oct 2015. doi: 10.1021/acs.analchem.5b02864.

[34] Justin Jefferies and Ribal Georges Sabat. Surface-relief diffraction gratings' optimization for plasmonic enhancements in thin-film solar cells. *Progress in Photovoltaics: Research and Applications*, 22(6):648–655, 2014. ISSN 1099-159X. doi: 10.1002/pip.2326.

[35] Mahmoud R. M. Atalla. Plasmonic absorption enhancement in a dye-sensitized solar cell using a fourier harmonics grating. *Plasmonics*, 10(1):151–156, 2015. doi: 10.1007/s11468-014-9789-x.

[36] Mahmoud R. M. Atalla. Multiple excitations of surface-plasmon-polariton waves in an amorphous silicon p-i-n solar cell using fourier harmonics and compound gratings. *J. Opt. Soc. Am. B*, 31(8):1906–1914, Aug 2014. doi: 10.1364/JOSAB.31.001906.

[37] Yan-Gang Bi, Jing Feng, Yang Chen, Yu-Shan Liu, Xu-Lin Zhang, Yun-Fei Li, Ming Xu, Yue-Feng Liu, Xiao-Chi Han, and Hong-Bo Sun. Dual-periodic-corrugation-induced broadband light absorption enhancement in organic solar cells. *Organic Electronics*, 27:167 – 172, 2015. doi: http://doi.org/10.1016/j.orgel.2015.09.021.

[38] Imran Khan, Hamid Keshmiri, Florian Kolb, Theodoros Dimopoulos, Emil J. W. List-Kratochvil, and Jakub Dostalek. Multidiffractive broadband plasmonic absorber. *Advanced Optical Materials*, 4(3):435–443, 2016. ISSN 2195-1071. doi: 10.1002/adom.201500508.

[39] Qiaoqiang Gan and Filbert J. Bartoli. Surface dispersion engineering of planar plasmonic chirped grating for complete visible rainbow trapping. *Applied Physics Letters*, 98(25):251103, 2011. doi: 10.1063/1.3601744.

[40] Guoxi Wang, Hua Lu, and Xueming Liu. Trapping of surface plasmon waves in graded grating waveguide system. *Applied Physics Letters*, 101(1):013111, 2012. doi: 10.1063/1.4733477.

[41] Chaolong Fang, Bo Dai, Zheng Li, Ali Zahid, Qi Wang, Bin Sheng, and Dawei Zhang. Tunable guided-mode resonance filter with a gradient grating period fabricated by casting a stretched pdms grating wedge. *Opt. Lett.*, 41(22): 5302–5305, Nov 2016. doi: 10.1364/OL.41.005302.

[42] Justin Kleingartner Wei-Hsun Yeh and Andrew C. Hillier. Wavelength tunable surface plasmon resonance-enhanced optical transmission through a chirped diffraction grating. *Analytical Chemistry*.

[43] Seyoon Kim, Yongjun Lim, Hwi Kim, Junghyun Park, and Byoungho Lee. Optical beam focusing by a single subwavelength metal slit surrounded by chirped dielectric surface gratings. *Applied Physics Letters*, 92(1):013103, 2008. doi: 10.1063/1.2828716.

[44] Luis Miguel Sanchez-Brea, Francisco Jose Torcal-Milla, and Tomas Morlanes. Near-field diffraction of chirped gratings. *Opt. Lett.*, 41(17):4091–4094, Sep 2016. doi: 10.1364/OL.41.004091.

[45] P. Rochon, E. Batalla, and A. Natansohn. Optically induced surface gratings on azoaromatic polymer films. *Applied Physics Letters*, 66(2):136–138, 1995. doi: 10.1063/1.113541.

[46] Robert Kirby, Ribal Georges Sabat, Jean-Michel Nunzi, and Olivier Lebel. Disperse and disordered: a mexylaminotriazine-substituted azobenzene derivative with superior glass and surface relief grating formation. *J. Mater. Chem. C*, 2:841–847, 2014. doi: 10.1039/C3TC32034K.

[47] D.J. Griffiths. *Introduction to Electrodynamics*. Prentice Hall, 1999. ISBN 9780138053260.

[48] Frank L Pedrotti, Leno Matthew Pedrotti, and Leno S. Pedrotti. *Introduction to optics*. Upper Saddle River, N.J. : Pearson Prentice Hall, 2007.

[49] M. Kuno. *Introductory Nanoscience*. Garland Science, 2012. ISBN 9780815344247.

[50] Peter W. Milonni and Joseph H. Eberly. *Laser Physics*. John Wiley and Sons, Inc., 2010. ISBN 9780470409718. doi: 10.1002/9780470409718.

[51] Eugene Hecht. *Optics (4th Edition)*. Addison Wesley, 4 edition, 2001. ISBN 0805385665.

[52] M.N.O. Sadiku. *Elements of Electromagnetics*. Oxf Ser Elec Series. Oxford University Press, 2010. ISBN 9780195387759.

[53] H. Raether. *Surface plasmons on smooth and rough surfaces and on gratings*. Number v. 111 in Springer tracts in modern physics. Springer, 1988. ISBN 9783540173632.

[54] Ribal Georges Sabat. Superimposed surface-relief diffraction grating holographic lenses on azo-polymer films. *Opt. Express*, 21(7):8711–8723, Apr 2013. doi: 10.1364/OE.21.008711.

[55] Cristina Cojocariu and Paul Rochon. Light-induced motions in azobenzene-containing polymers. *Pure and Applied Chemistry*, 76(7-8):1479–1497, 2004. doi: 10.1351/pac200476071479.

[56] Armando Giannattasio, Ian R. Hooper, and William L. Barnes. Transmission of light through thin silver films via surface plasmon-polaritons. *Opt. Express*, 12(24):5881–5886, Nov 2004. doi: 10.1364/OPEX.12.005881.

[57] P. B. Johnson and R. W. Christy. Optical constants of the noble metals. *Phys. Rev. B*, 6:4370–4379, Dec 1972. doi: 10.1103/PhysRevB.6.4370.

[58] Philip E. Ciddor. Refractive index of air: new equations for the visible and near infrared. *Appl. Opt.*, 35(9):1566–1573, Mar 1996. doi: 10.1364/AO.35.001566.

[59] G. Winter and W. L. Barnes. Emission of light through thin silver films via near-field coupling to surface plasmon polaritons. *Applied Physics Letters*, 88(5):051109, 2006. doi: 10.1063/1.2170426.

[60] W. L. Barnes, T. W. Preist, S. C. Kitson, and J. R. Sambles. Physical origin of photonic energy gaps in the propagation of surface plasmons on gratings. *Phys. Rev. B*, 54:6227–6244, Sep 1996. doi: 10.1103/PhysRevB.54.6227.

[61] Yan-Gang Bi, Jing Feng, Yu-Shan Liu, Yun-Fei Li, Yang Chen, Xu-Lin Zhang, Xiao-Chi Han, and Hong-Bo Sun. Surface plasmon-polariton mediated red emission from organic light-emitting devices based on metallic electrodes integrated with dual-periodic corrugation. *Scientific Reports*, 4 (7108), 2014. doi: 10.1038/srep07108.

[62] James Leibold and Ribal Georges Sabat. Laser-induced controllable chirped-pitch circular surface-relief diffraction gratings on azo glass. *Photon. Res.*, 3 (4):158–163, Aug 2015. doi: 10.1364/PRJ.3.000158.

Appendix

A Papers published from research

Erin Bailey and Ribal Georges Sabat, "Surface plasmon bandwidth increase using chirped-pitch linear diffraction gratings," Opt. Express 25, 6904-6913 (2017)